

RR-86-112

AD-A221 563

Technical Memorandum

SAR DETECTION OF SHIP- GENERATED TURBULENT AND VORTEX WAKES

J.D. LYDEN
D.R. LYZENGA
R.A. SHUCHMAN
Radar Division

C.V. SWANSON
Applied Physics Technology, Inc.
1800 Old Meadow Road, Suite 120
McLean, VA 22102

SEPTEMBER 1985

DTIC
ELECTE
APR 30 1990
S E D

ENVIRONMENTAL

RESEARCH INSTITUTE OF MICHIGAN

1000 S. ZEEB ROAD, ANN ARBOR, MICHIGAN 48107

Best Available Copy

ABSTRACT

A frequently observed ship wake feature in Synthetic Aperture Radar (SAR) images is a dark, narrow line along the ship track. These features have been termed turbulent wakes, although it is not clear that turbulence alone is responsible for their appearance. It has been suggested that vortices produced by the ship's hull may be responsible for the suppression of surface waves near the ship track and an enhancement of the waves near the edge of the smoothed area.

The primary purpose of the study reported here was to use a hydrodynamic model for ship-generated vortices as input to existing radar backscatter models, and to use this hybrid model to produce simulated SAR ship wake signatures for comparison with actual measurements. For the limited number of cases considered, the simulated wake signatures agreed closely to those observed in actual SAR data. Our results also indicated that the SAR signatures are related to the vortex currents under low wind conditions and to the strain rates associated with the ship-generated vortices under high winds.

Additional studies included the radar resolution dependence of SAR ship wake features as well as examination of the Fourier transform of a ship wake image for information which could be used in an automatic detection algorithm.

DTIC
ELECTE
APR 30 1990
S 3 D

DISTRIBUTION STATEMENT A

Approved for public release;
Distribution Unlimited

PAGES _____
ARE
MISSING
IN
ORIGINAL
DOCUMENT

TABLE OF CONTENTS

ABSTRACT	i
LIST OF FIGURES	v
LIST OF TABLES	ix
1. INTRODUCTION	1
2. SAR MODELING OF VORTEX WAKES	7
2.1 Hydrodynamic Models	7
2.1.1 Vortex Wake Model	7
2.1.2 Wave-Current Interactions	13
2.2 Model Results	15
2.2.1 Detailed Comparison	15
2.2.2 Modeled Predictions	21
2.3 Additional Imagery	35
2.4 Resolution Effects	45
2.5 Detection Applications	48
3. CONCLUSIONS AND RECOMMENDATIONS	55
APPENDIX A: SAR DETECTABILITY OF SURFACE WAVE PERTURBATIONS	59
REFERENCES	67

Accession For	
NTIS GRA&I	<input checked="" type="checkbox"/>
DTIC TAB	<input type="checkbox"/>
Unannounced	<input type="checkbox"/>
Justification	
By <i>per Form 50</i>	
Distribution/	
Availability Codes	
Dist	Avail and/or Special
<i>A-1</i>	

LIST OF FIGURES

1. Overview of Ship Wake Generation Mechanisms	2
2. Simultaneously Obtained L- and X-Band Optical SAR Imagery of a Turbulent Wake Feature	4
3. Diagram of Turbulent Wake Structure Showing Possible Role of Vortices and Net Rearward Velocity Within Turbulent Region (after Swanson, 1984)	5
4. Overview of Hydrodynamic Flow in Wake of Ship (from Swanson, 1984)	8
5. Schematic Showing How Velocity Increases and Pressure Decreases Beneath Hull of Displacement Ship (from Swanson, 1984)	10
6. Definition of Model Coordinates (from Swanson, 1984)	12
7. L-Band Digital SAR Image Collected During the 1983 Georgia Strait Experiment; the Location Where Backscatter Measurements were Performed is Indicated by the Line A-A'	17
8. Radar Backscatter Scan Across A'-A as Shown on Figure 7	18
9. (a) Surface Currents Calculated for Line A-A' Shown in Figure 7, and (b) Spectral Perturbations of 30 cm Waves for the Current Profile in (a)	19
10. Graphical Comparison of Predicted Radar Backscatter Variation Based on Vortex Model (dashed) and Actual Backscatter Measurements (solid)	20
11. Decay of Wake-Induced Surface Currents as a Function of Distance Behind Generating Ship (from Swanson, 1984)	23

LIST OF FIGURES (Continued)

12.	Modeled Vortex-Produced Surface Currents One Kilometer Behind a 5000 ton Ship (Case 1)	25
13.	Modeled Detectability of the Vortex-Produced Surface Currents in Figure 11 as a Function of Wavelength and Wind Speed	26
14.	Modeled Vortex-Produced Surface Currents Five Kilometers Behind a 500 Kiloton Ship (Case 3)	28
15.	Perturbations Caused by the Vortex-Produced Surface Currents in Figure 14 as a Function of Wavelength and Wind Speed	29
16.	Modeled Vortex-Produced Surface Currents Ten Kilometers Behind a 500 Kiloton Ship (Case 3)	32
17.	Modeled Perturbations of the Vortex-Produced Surface Currents in Figure 16 as a Function of Wavelength and Wind Speed	33
18.	Modeled Perturbations of Vortex-Produced Wakes for Case 3 as a Function of Wavelength, Wind Speed, and Distance Aft of the Ship	34
19.	L- and X-Band Optical SAR Imagery of a Turbulent Wake Feature Collected 2 November 1978	36
20.	Estimated Surface Current Profile and Modeled Spectral Perturbations for L-Band Bragg Waves Corresponding to Figure 19	38
21.	Estimated Surface Current Profile and Modeled Spectral Perturbations for X-Band Bragg Waves Corresponding to Figure 19	39
22.	X-Band Optical SAR Image Indicating Turbulent Wake Splitting (Pass 2, 3 November 1978)	40
23.	Seasat SAR Image of Suspected Oil Tanker in the Gulf of Alaska (after Fu and Holt, 1982)	41

LIST OF FIGURES
(continued)

24.	X-Band Optical SAR Imagery Collected During Very Low Wind Conditions of (a) a Relatively Fast Moving Ship, and (b) Slow Moving Ships	43
25.	X-Band Optical SAR Image Indicating Wave Breaking Due to Vortex Current Interactions	44
26.	L-Band Digital Aircraft SAR Data Processed to (a) Full Resolution, and (b) Simulated Seasat Resolutions	46
27.	Coincident L-Band SAR Imagery Collected by (a) Aircraft, and (b) Seasat	47
28.	L-Band Ship Wake SAR Image Used in Detection Studies	49
29.	Fast Fourier Transform Magnitude Spectrum of SAR Image Shown in Figure 28	50
30.	Subset of Ship Wake Image Shown in Figure 28 Used in Detection Studies	52
31.	Fast Fourier Transform Magnitude Spectrum of SAR Image Shown in Figure 30	53
A-1.	Spectral Perturbation Pattern Used in SAR Simulation	60
A-2.	One-Look Simulated SAR Image Illustrating the Detectability of Wake Features as a Function of Spectral Perturbation and Width	61
A-3.	Four-Look Simulated SAR Image Illustrating the Detectability of Wake Features as a Function of Spectral Perturbation and Width	63
A-4.	Higher Resolution One-Look Simulated SAR Image Illustrating the Detectability of Wake Features as a Function of Spectral Perturbation and Width	65

LIST OF TABLES

1. Summary of Ship Parameters Used in Vortex Simulations 22

1 INTRODUCTION

Ship wake patterns exhibiting a wide diversity of appearance have been noted on Synthetic Aperture Radar (SAR) images collected with various systems under a broad range of environmental conditions. As a result of a careful examination of the available data and a cataloging of these observations, in addition to several recent theoretical analyses, it appears that the wake structures within the existing body of observational data can be classified into three general categories of phenomena as shown in Figure 1. These categories include: (1) surface waves generated directly by the ship, (2) turbulent wakes or vortices containing relatively persistent but non-propagating currents, which are visible by SAR through the interaction of ambient waves with these surface currents, and (3) internal waves generated by the ship, which again are visible because of their interactions with short surface waves. ERIM is actively involved in all three phases of SAR ship wake studies. An earlier study (Lyden, et al., 1985a), carefully examined the SAR imaging characteristics of ship-generated surface waves. That study indicated that the bright, narrow V-wakes observed behind ships under low wind conditions could be adequately explained by a first-order Bragg scattering mechanism. ERIM has also performed research into ship-generated internal waves (Lyden, 1985b).

The purpose of the study reported here has been to investigate the narrow dark bands frequently observed in SAR imagery extending behind moving ships. These features occur when the ocean surface is sufficiently rough to yield a measurable radar return, which is suppressed in the region near the ship track. The suppression is frequently more pronounced at L-band (23.5 cm wavelength) than at X-band (3.2 cm wavelength), and is sometimes accompanied by a bright line on one or both edges of the dark area. An example of these

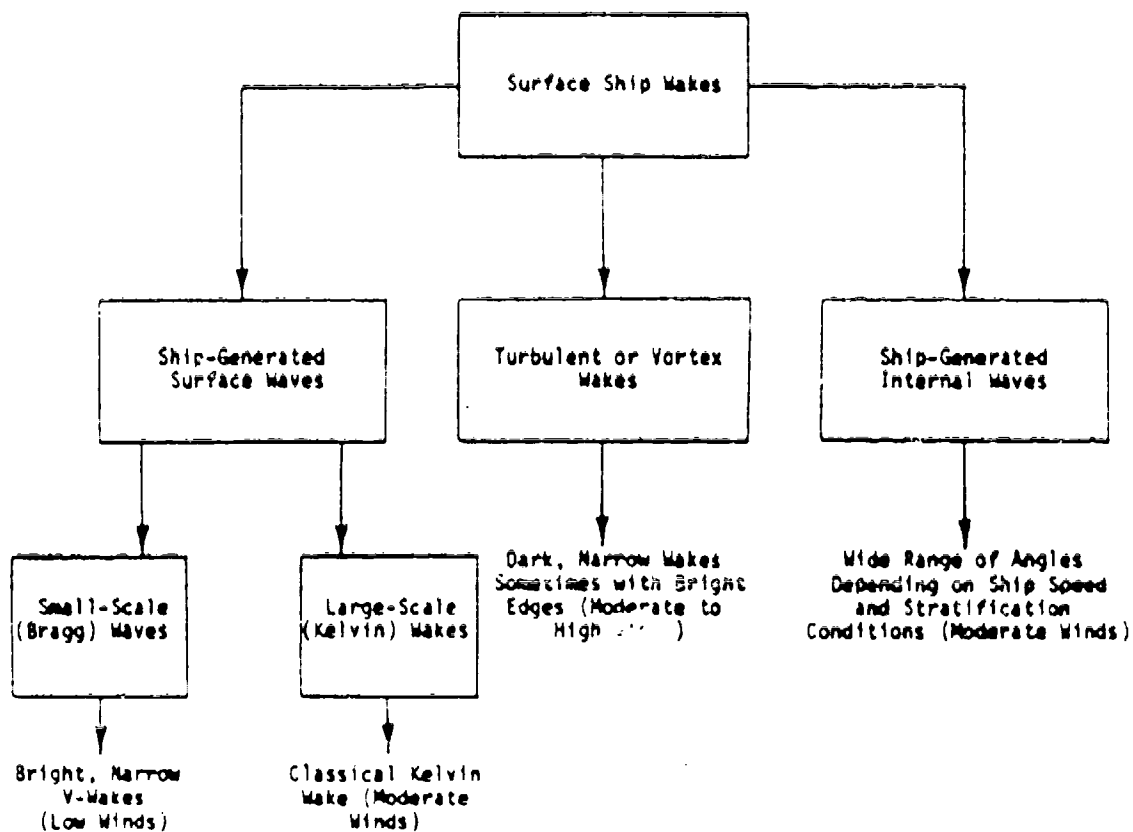


Figure 1. Overview of Ship Wake Generation Mechanisms

features is shown in Figure 2 for simultaneously obtained L- and X-band imagery.

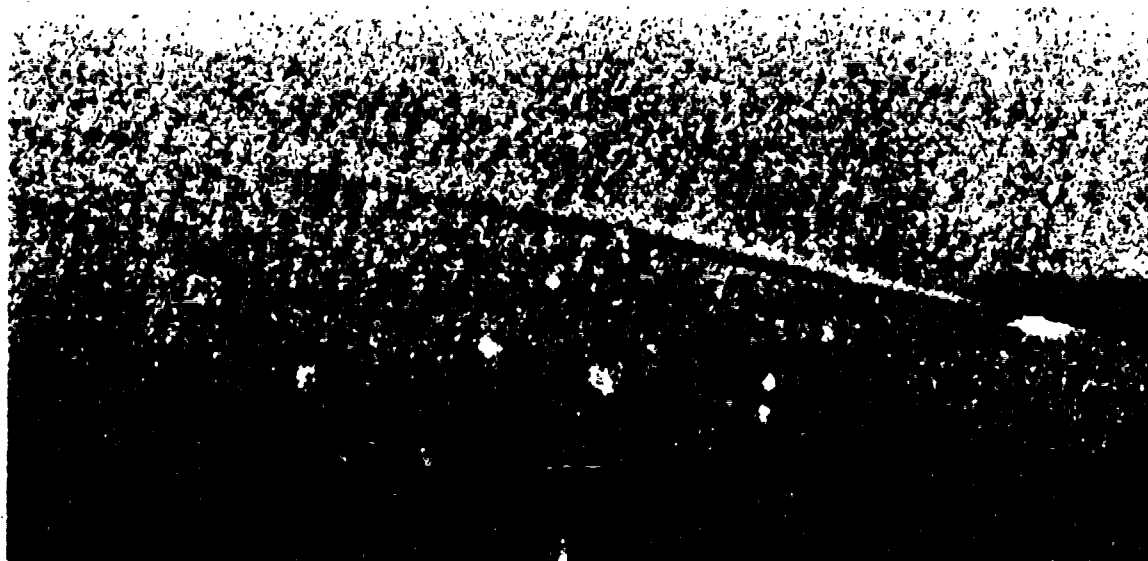
The features described above have been termed turbulent wakes (Shuchman, et al., 1983), although it is not clear that turbulence alone is responsible for the appearance of these features. The effects of turbulent currents on surface waves are not well understood and the persistence of the phenomenon is somewhat problematic. It has been suggested that horizontal vortices produced at the edges of the ship's hull, as well as a net rearward velocity within the turbulent wake, may be responsible for the suppression of surface waves near the ship track and an enhancement of the waves near the edges of the smoothed area (Swanson, 1984). These characteristics are shown graphically in Figure 3. The vortex mechanism would also help explain the persistence of turbulent wake features in SAR imagery. Turbulent wake features have been observed extending up to 20 km aft of the generating ship in Seasat imagery.

In this study, a first attempt is made at using a hydrodynamic model for these vortices as input to existing radar backscatter models, and to use this hybrid model to produce simulated SAR wake signatures for comparison with actual measurements. Presented below is a description of the hydrodynamic and radar backscatter models we employed. This is followed by a detailed quantitative comparison for a single data set which appears to validate the application of this model.

The model was then exercised to predict the expected SAR signature for several hypothetical ship, SAR, and environmental conditions. These results can be used to aid in the design of an optimum SAR system for the detection of these wakes. This is followed by a presentation of several SAR images which appear to qualitatively agree with model predictions. Also presented in this report is an investigation into the effects of SAR resolution on ship wake



WIND (7 m/s)



X-Band

1 km

Figure 2. Simultaneously Obtained L- and X-Band Optical SAR Imagery of a Turbulent Wake Feature

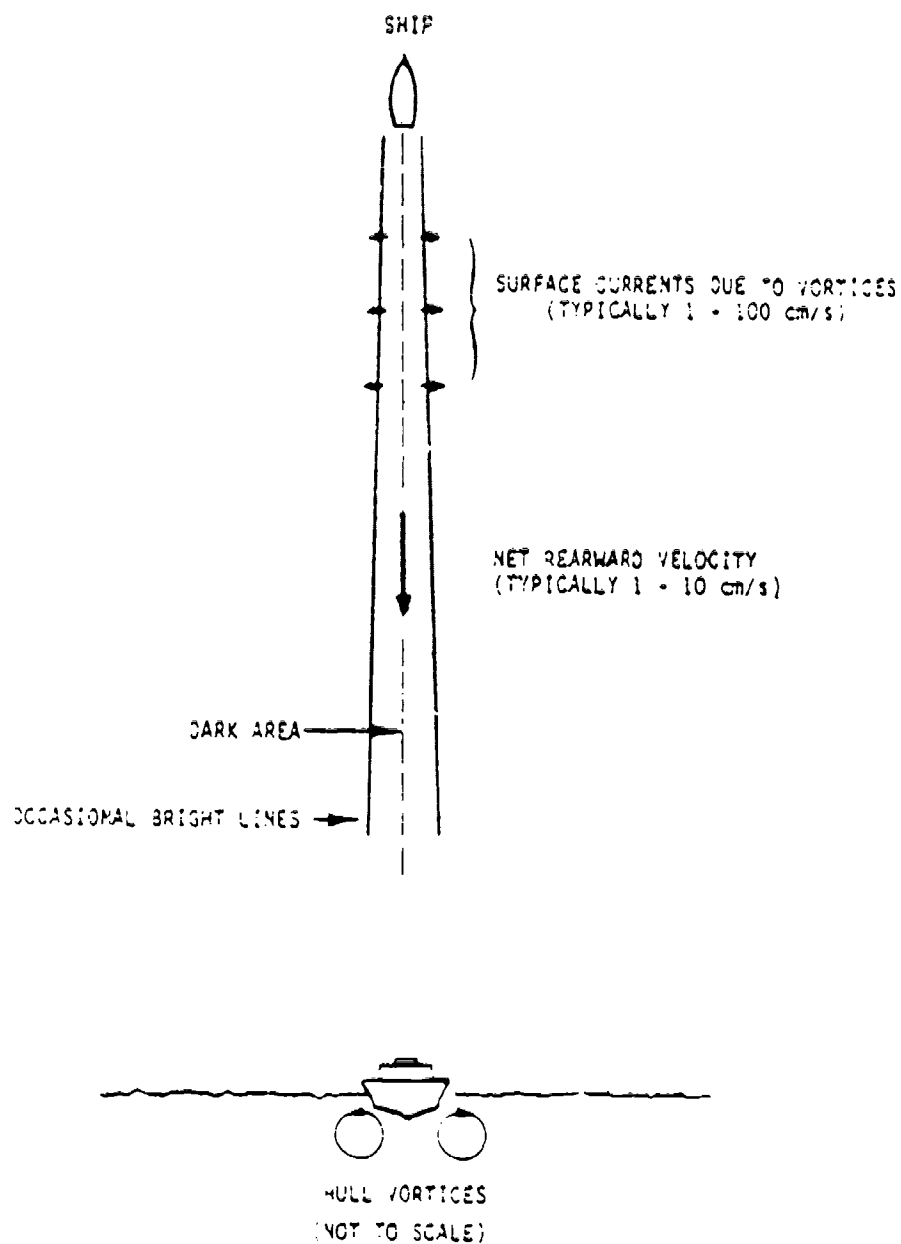


Figure 3. Diagram of Turbulent Wake Structure Showing Possible Role of Vortices and Net Rearward Velocity Within Turbulent Region (after Swanson, 1984)

detection as well as a study on the use of the Fourier transform of a SAR ship wake image for detection applications. Finally, a conclusions and recommendations section is presented. Included as an appendix is a discussion on the detectability of surface patterns in SAR imagery.

2 SAR MODELING OF VORTEX WAKES

In this section, a description of the hydrodynamic model for the vortex wakes is given as well as a description of the radar backscatter model we utilized in our simulations. This is followed by a quantitative comparison of a simulated wake signature with actual measurements for a case where the various ship and environmental parameters were well known. A series of simulations were also performed to help determine an optimum SAR configuration for the detection of vortex wake features. Several SAR images of turbulent wake features are also presented which qualitatively support the vortex mechanism. Finally, a brief investigation of the effects of SAR resolution on ship wake detection is presented, as well as a discussion on using the Fourier transform of a ship wake image for detection purposes.

2.1 HYDRODYNAMIC MODELS

The hydrodynamic aspects of our study can be grouped into two categories. The first is the manifestation of surface currents through vortex generation. The second is the interaction of these currents with the short-scale Bragg waves which produce the radar backscatter. Each of these topics is discussed below.

2.1.1 VORTEX WAKE MODEL

The components of the proposed vortex wake model are illustrated in Figure 4. In this figure, a ship is shown travelling through the water at steady speed U_s . It radiates a Kelvin wake, which carries away forward momentum. The turbulent wake produced by the ship therefore must have a net rearward momentum, as shown in the figure. In addition, a vortex pair is produced by the ship hull, which causes a change in the lateral flow field behind the ship. And finally,

Wake Flow of Ship

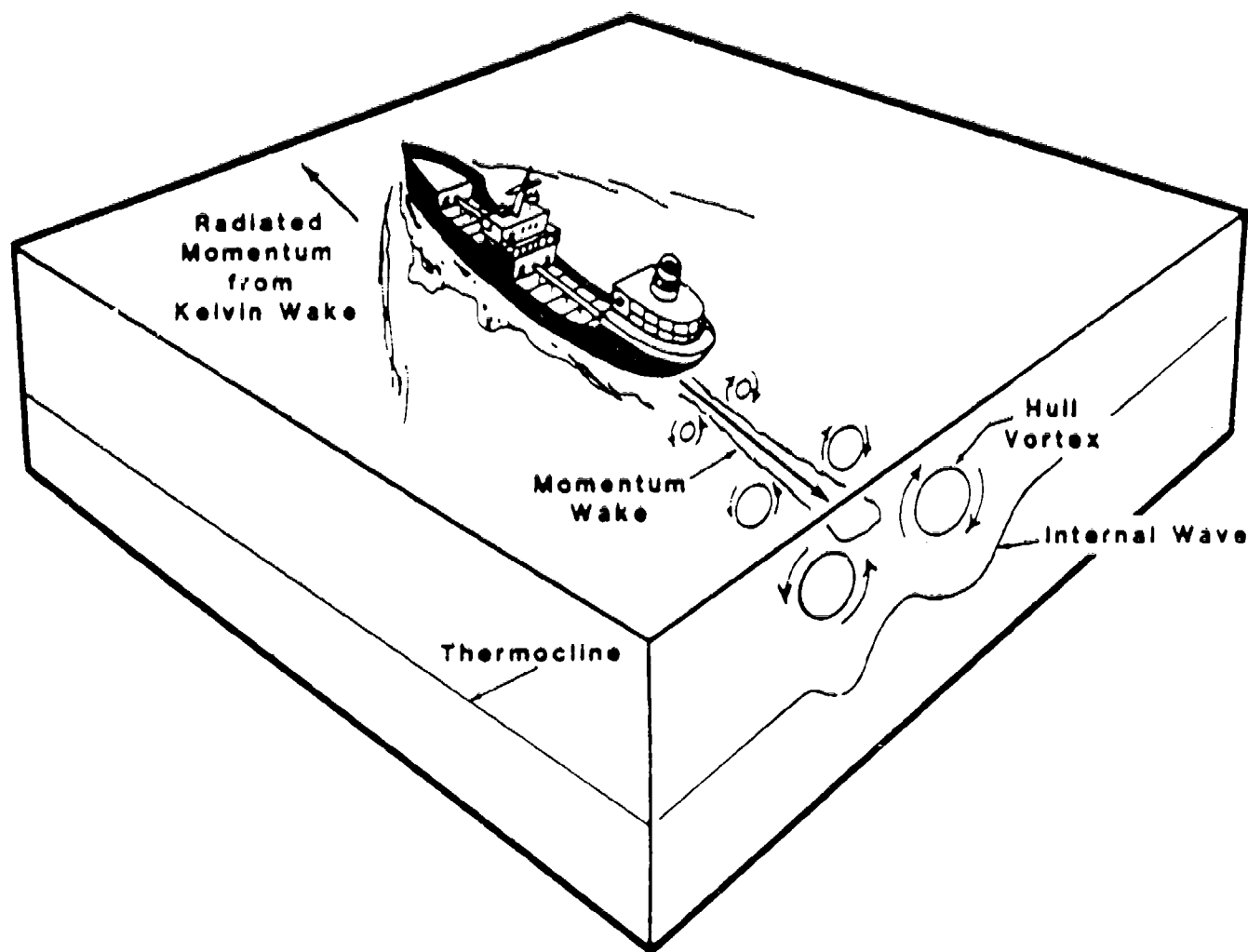


Figure 4. Overview of Hydrodynamic Flow in Wake of Ship
(from Swanson, 1984)

when a strong thermocline is present, the flow field of the vortex pair can interact with it, causing pressure and velocity changes at depths which generate internal waves. All of these hydrodynamic phenomena give rise to horizontal currents at the ocean surface which interact with surface waves to produce changes in surface roughness which are potentially detectable by SAR. The present report considers only the effects of the vortex pair.

A ship generates a flow field due to a vortex pair which is produced and shed by the hull. In all displacement ships, the water must accelerate as it passes around the bottom of the ship hull, as illustrated in Figure 5. This gives rise to a pressure drop along the bottom of most of the hull, due to the Bernoulli Effect. This effect has been confirmed on ship hulls by numerous measurements, and gives rise to a negative lift, or downward force which is well-known to naval architects as "sinkage-in-trim" or "squat." This force causes the ship to ride lower in the water at higher speeds.

This force L can be described approximately by

$$L = (\rho \ell) \frac{\rho}{2} C_p U_s^2, \quad (1)$$

where d is the ship beam, ℓ its length, ρ the water density, U_s the ship speed, and C_p a coefficient between 0.1 and 0.01, depending on hull shape. The coefficient C_p has been estimated as

$$C_p = 1.5 \left(\frac{d}{\ell} \right)^{3/2}. \quad (2)$$

From the theory of lift, it can be shown that this force must give rise to the shedding of at least one vortex pair, and the total circulation Γ in the vortex must be

$$\Gamma = \frac{L}{\rho U_s f} = \frac{C_p U_s \ell}{2f}, \quad (3)$$

where f is a constant approximately equal to 0.75, arising from the distribution of lift on the hull of the ship.

Origin of Bernoulli Pressure Drop

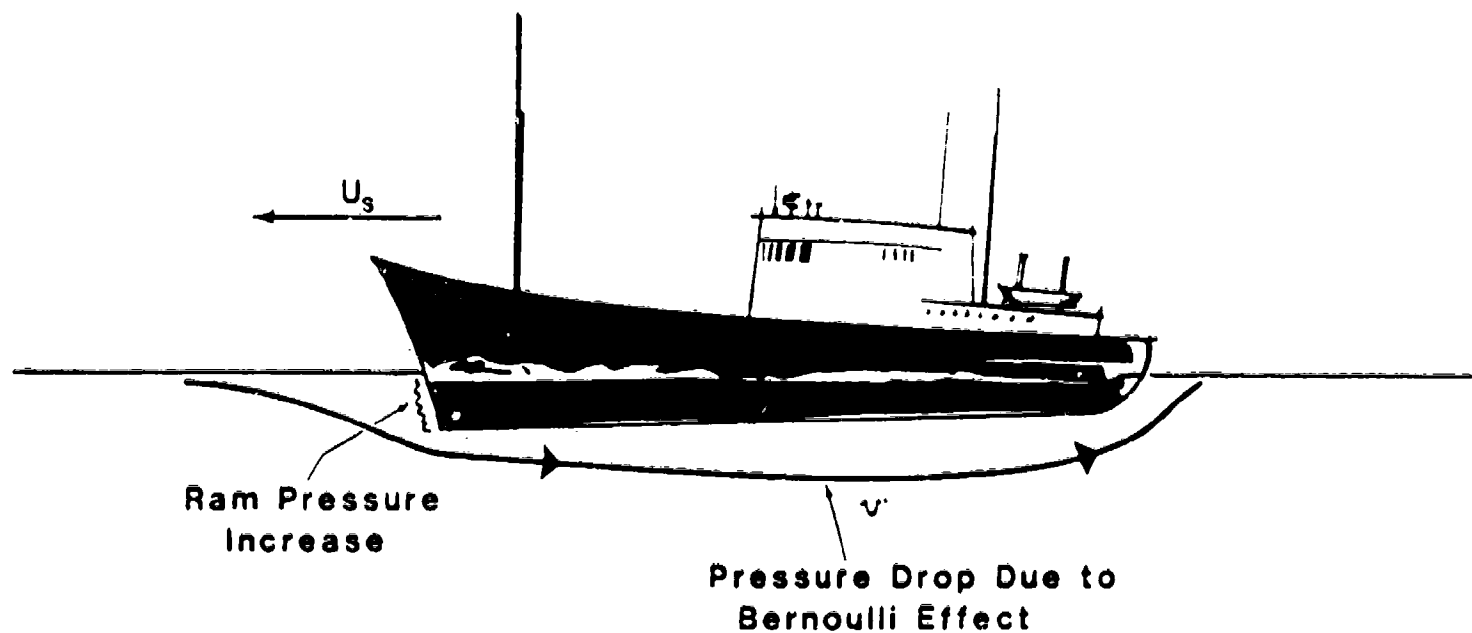


Figure 5. Schematic Showing How Velocity Increases and Pressure Decreases Beneath Hull of Displacement Ship (from Swanson, 1984)

The definition of circulation Γ is that it is the total integrated vorticity per unit length along track in one of the vortices. When the vorticity in such a vortex is highly localized in the vortex core, the velocity flow field due to the vortex can be described very simply as a tangential velocity field V_θ by

$$V_\theta = \frac{\Gamma}{2\pi r} , \quad (4)$$

where Γ is the circulation in the vortex, and r is the radius to the vortex center.

The vortices shed by the hull will have the geometry and orientation shown in Figure 6. This will produce upwash in the center of the wake behind the ship, and generate a spreading or diverging flow in the wake center at the surface. This lateral surface velocity is designated V_y .

Because the boundary condition for the water surface is that the flow must be primarily horizontal, a pair of image vortices are required above the surface to satisfy this condition. The interaction of the hull vortices with their images causes a lateral motion of the hull vortices away from one another. The lateral spreading speed V_c of the hull vortex core will be

$$V_c = \frac{\Gamma}{4\pi z} = \frac{\Gamma}{2\pi} \frac{1}{df} . \quad (5)$$

Here, z is the equilibrium depth of the vortex. It can be shown that each vortex comes to an equilibrium depth of about $d/2$, which is very close to the depth at which it is produced, and consequently its motion after shedding is primarily horizontal.

The resulting lateral velocity field V_y at the surface will be given by

$$V_y = \frac{\Gamma}{\pi} \left[\frac{z}{z^2 + (y - b/2)^2} - \frac{z}{z^2 + (y + b/2)^2} \right] , \quad (5')$$

Coordinate System for Hull Vortices

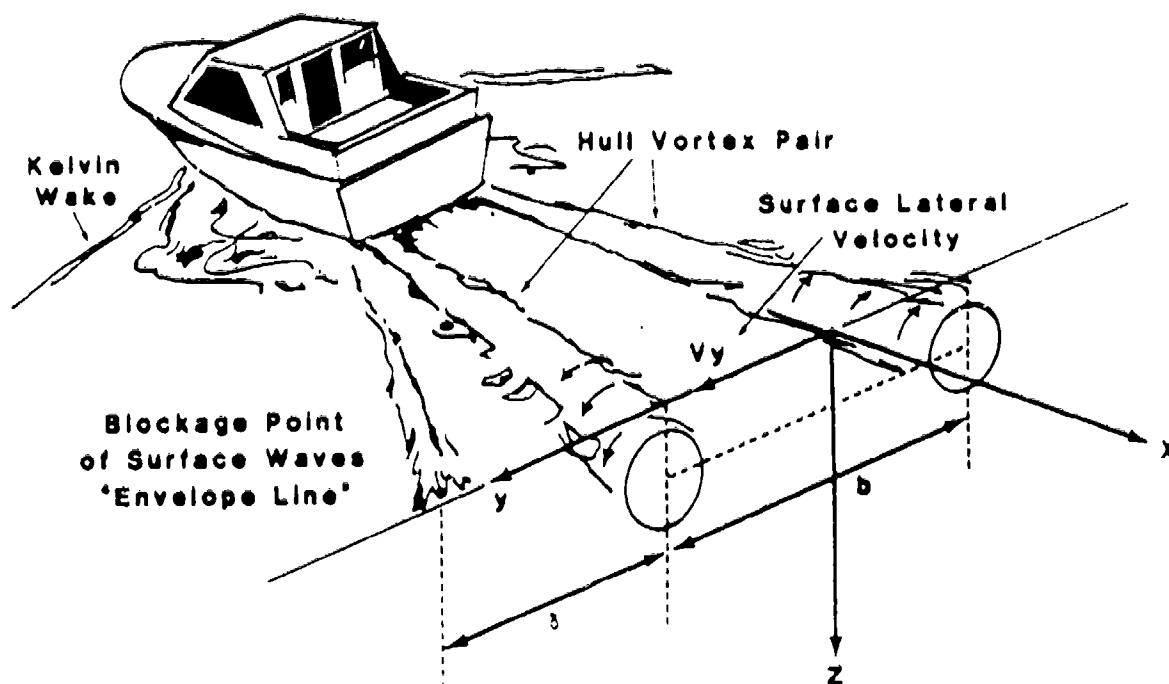


Figure 6. Definition of Model Coordinates (from Swanson, 1984)

where b is the lateral separation distance between the vortices, z is the depth of the vortices, and y is the lateral distance from wake centerline on the surface. As a result of this analysis, we see that the vortex pair generates a lateral spreading velocity on the surface behind the ship, and this current will also have an effect on the amplitude of any surface waves which are present, thereby offering possibility of detection by SAR. The interaction of these vortex-induced surface currents with small-scale surface waves will be discussed in the next section.

2.1.2 WAVE-CURRENT INTERACTIONS

The microwave reflectivity of the ocean surface is primarily a function of the small-scale (centimeters and decimeters) surface roughness. For incidence angles between about 20° and 70° , Bragg scattering is believed to be the dominant scattering mechanism. The Bragg scattering model yields a radar cross section per unit area (for the backscatter case with the plane of incidence perpendicular to the y -axis) of

$$\sigma_0(\theta) = 4\pi k^4 \cos^4 \theta |g_{ij}(\theta)|^2 W(2k \sin \theta, 0), \quad (7)$$

where k is the electromagnetic wavenumber, θ is the incidence angle, $W(k_x, k_y)$ is the wave height spectral density, and $g_{ij}(\theta)$ are scattering coefficients (Valenzuela, 1978). Thus, to first order, the backscattered power is proportional to the surface wave spectral density at the Bragg wavenumber

$$\vec{k}_B = (2k \sin \theta, 0). \quad (8)$$

For the purposes of our wake studies, we are interested in the change of spectral density of Bragg waves at each point in the vortex-produced current pattern and whether these changes are observable by a SAR.

To achieve this, a computer program has been written and implemented on a Zenith Model 100 microcomputer. This program was initially written for use in internal wave studies and is described in detail by Lyzenga (1984). In summary, this program solves for an initial wavelength outside the current pattern corresponding to the Bragg waves at each point in the current pattern. The program calculates the change in spectral density for these waves due to current interactions. The basis for these calculations is the conservation of wave action spectral density (Phillips, 1977) which is defined as

$$N = \frac{F}{\omega}, \quad (9)$$

where F is the wave height spectrum and ω is the radian wave frequency [$\omega = (gk)^{1/2}$]. The wave height spectral density at equilibrium is assumed to be given by the Phillips spectrum

$$F_0(k) = Ak^{-4} \quad (10)$$

so the wave action spectral density at equilibrium is

$$N_0(k) = Ag^{-1/2}k^{-4.5}. \quad (11)$$

The deviation from the equilibrium state is specified by the spectral perturbation f , which is defined as

$$f = \frac{N(k) - N_0(k)}{N_0(k)}. \quad (12)$$

Note that this perturbation function applies to the wave height spectrum as well, thus, the perturbation is directly related to the expected change in radar backscatter based on a Bragg scattering model [Eq. (7)]. To relate this perturbation value to the more commonly used backscatter change in decibels, one would simply use the relationship

$$\Delta\sigma_{dB} = 10 \left[\log_{10}(1 + f) \right]. \quad (13)$$

Several points should be clarified regarding this approach. The initial wave conditions are based on a Phillips spectrum, which assumes that the waves are saturated. This may not be true at low wind speeds. Also, it is not clear how much waves can grow beyond saturation before the onset of breaking. This would minimize the effects of positive perturbations calculated by our model. It should be mentioned that the wind growth/relaxation rates used in our model were based on the work of Hughes (1978). Finally, we should note that only transverse currents associated with the ship-generated vortices have been considered. We have not included the effects of the nearward axial current in this work.

2.2 MODEL RESULTS

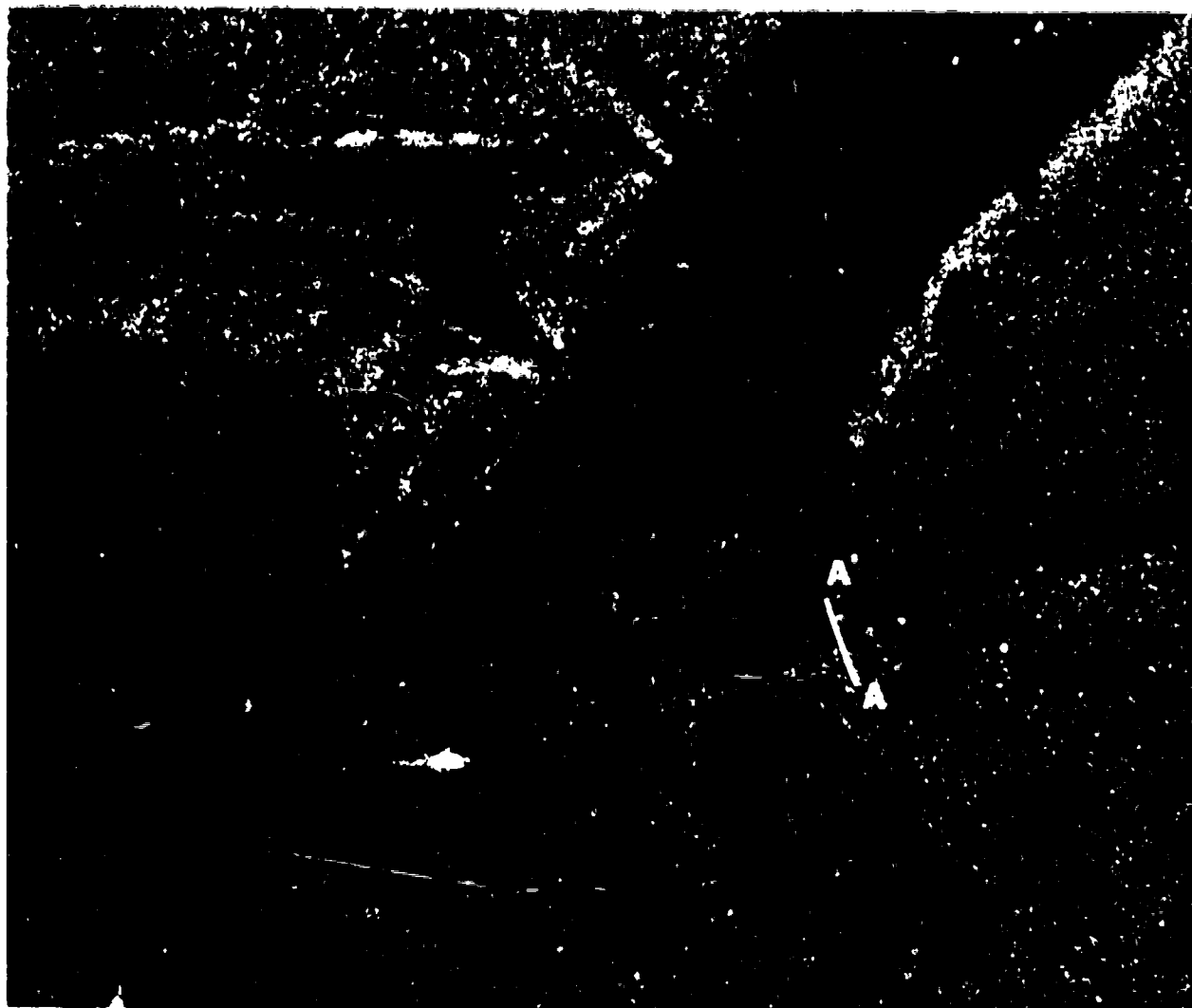
Included in this section is a detailed comparison between our model predictions and actual measurements made on data collected during the 1983 Georgia Strait Experiment. Also included are a series of model calculations of wake detectability for a variety of ship, radar, and environmental parameters. These results can be used to determine an optimum sensor configuration for vortex wake detection. Finally, several SAR images of ship wakes are presented and discussed within the context of the vortex wake model.

2.2.1 DETAILED COMPARISON

Although there exists a great deal of SAR imagery containing snips and turbulent wake-like features, there are very few cases where the wake-generating ship parameters and wind conditions were well documented. One exception is the SAR data collected during the 1983 Georgia Strait Experiment. The required ship parameters for our model are length, beam, and speed. Surface wind speed and direction are also necessary inputs. During portions of the Georgia Strait Experiment, the Navy tug Guapaw was making controlled runs as part of a snip wake study. During these runs, the ship speed was held constant and the surface wind conditions were monitored.

Presented in Figure 7 is an L-band image of the Quapaw and its wake which was collected during the 1983 Georgia Strait Experiment. The stern waves and turbulent wake generated by the Quapaw are clearly visible. The approximate wind conditions during this run are shown graphically on the image. One kilometer aft of the ship's location along the line A-A' indicated on Figure 7, radar backscatter values were extracted and are shown plotted in Figure 8. These measurements indicate a peak in radar intensity at the upwind edge of the wake feature which is about 11 dB above the minimum intensity level at the wake center. A simulation of this wake was performed corresponding to this location. The parameters we used in this simulation were consistent with the Quapaw's during the run and were based on the fast vortex decay model discussed by Swanson (1984). We allowed the separation of the vortices [b in Eq. (6)] to vary to match the width of the observed wake feature. The surface current profile for this simulation is shown in Figure 9(a). The corresponding spectral perturbations which were simulated for this case are presented in Figure 9(b). These were generated for a surface wavelength of 30 cm which is approximately the Bragg wavelength for the data studied. Figure 9(b) can be interpreted as the wind and waves both traveling from right to left entering the current pattern plotted in Figure 9(a). These results indicate a strong positive perturbation at the location of the maximum adverse current, and a maximum negative perturbation where the waves and current are in the same direction and the current is a maximum. Downwind of this point, the waves gradually return to equilibrium.

A comparison between the predicted and actual radar intensities for this wake feature is shown in Figure 10. The simulated radar intensities were obtained by converting the spectral perturbations shown plotted in Figure 9(a) to equivalent backscatter changes in decibels using the relationship given previously as Eq. (13). The vertical and horizontal position of the two plots was adjusted to



1 km

Figure 7. L-Band Digital SAR Image Collected During the 1983 Georgia Strait Experiment; the Location Where Backscatter Measurements were Performed is Indicated by the Line A-A'

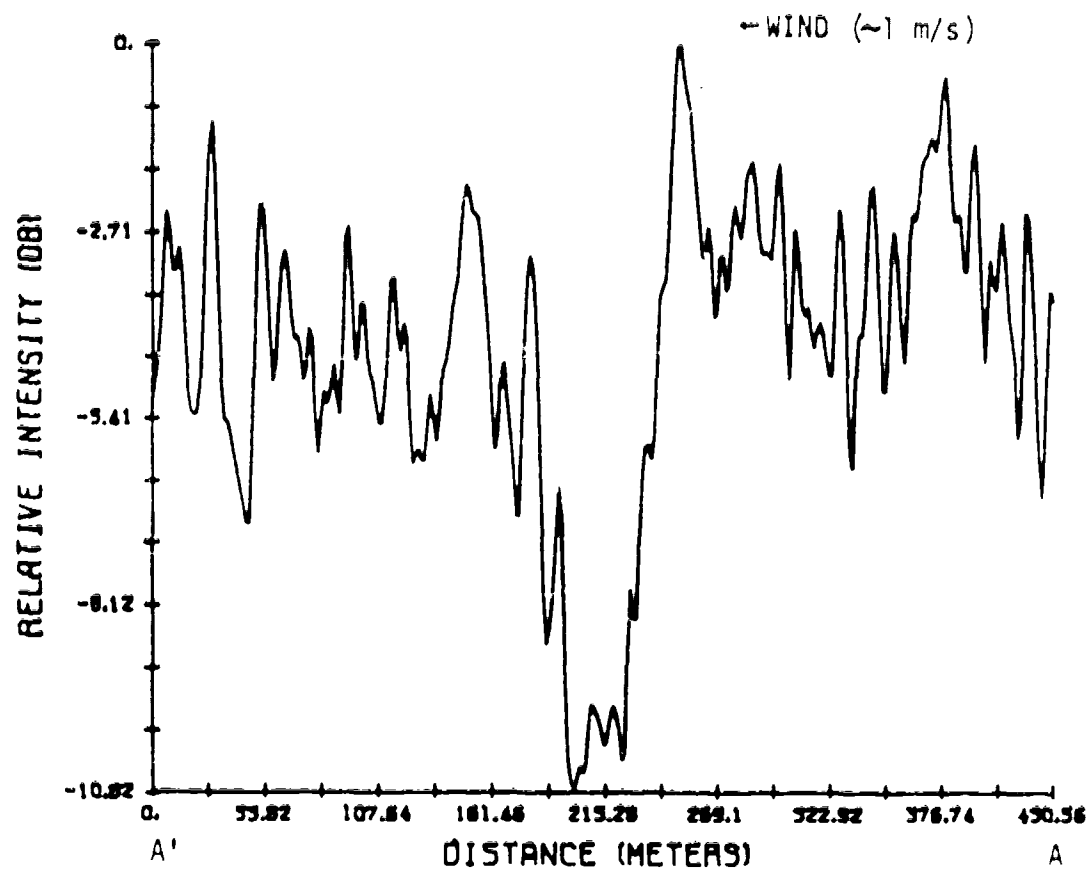


Figure 8. Radar Backscatter Scan Across A'-A as Shown on Figure 7

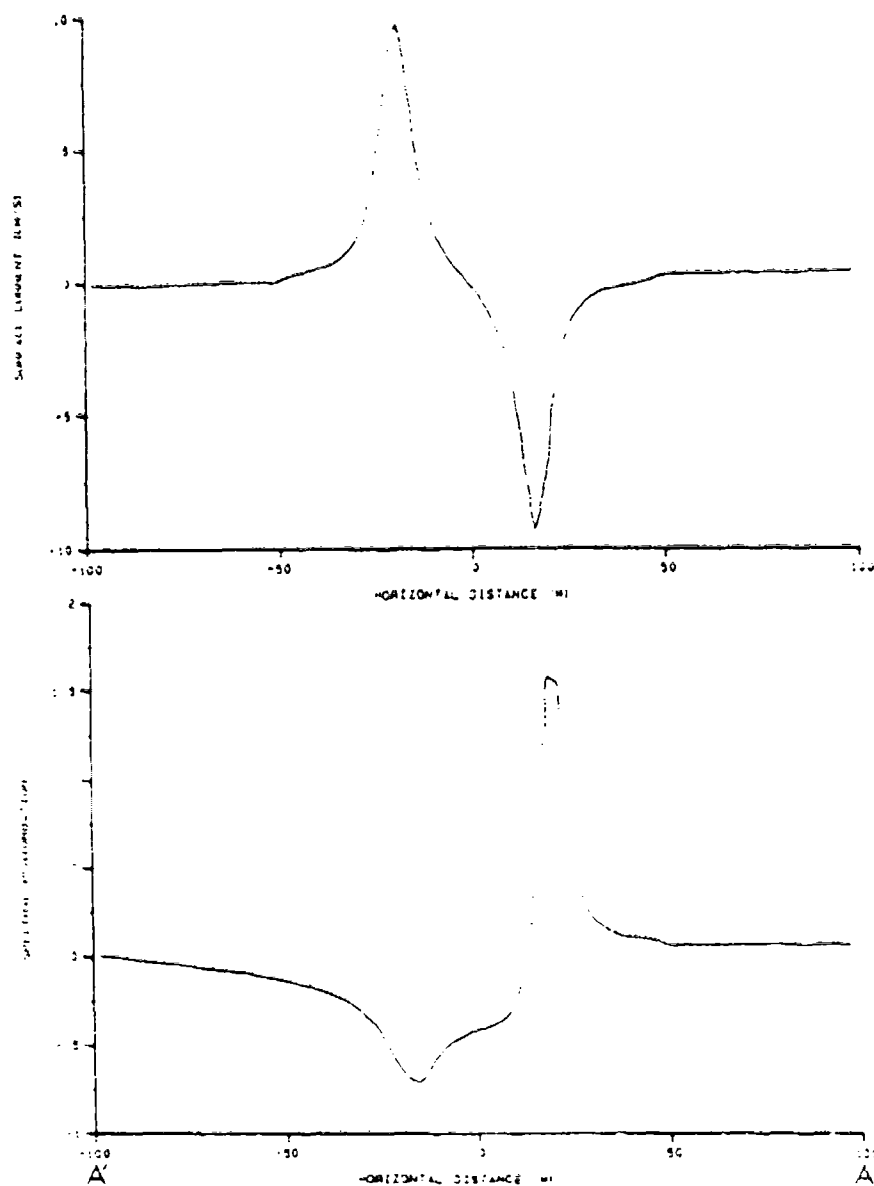


Figure 9. (a) Surface Currents Calculated for Line A-A' Shown in Figure 7, and (b) Spectral Perturbations of 30 cm Waves for the Current Profile in (a)

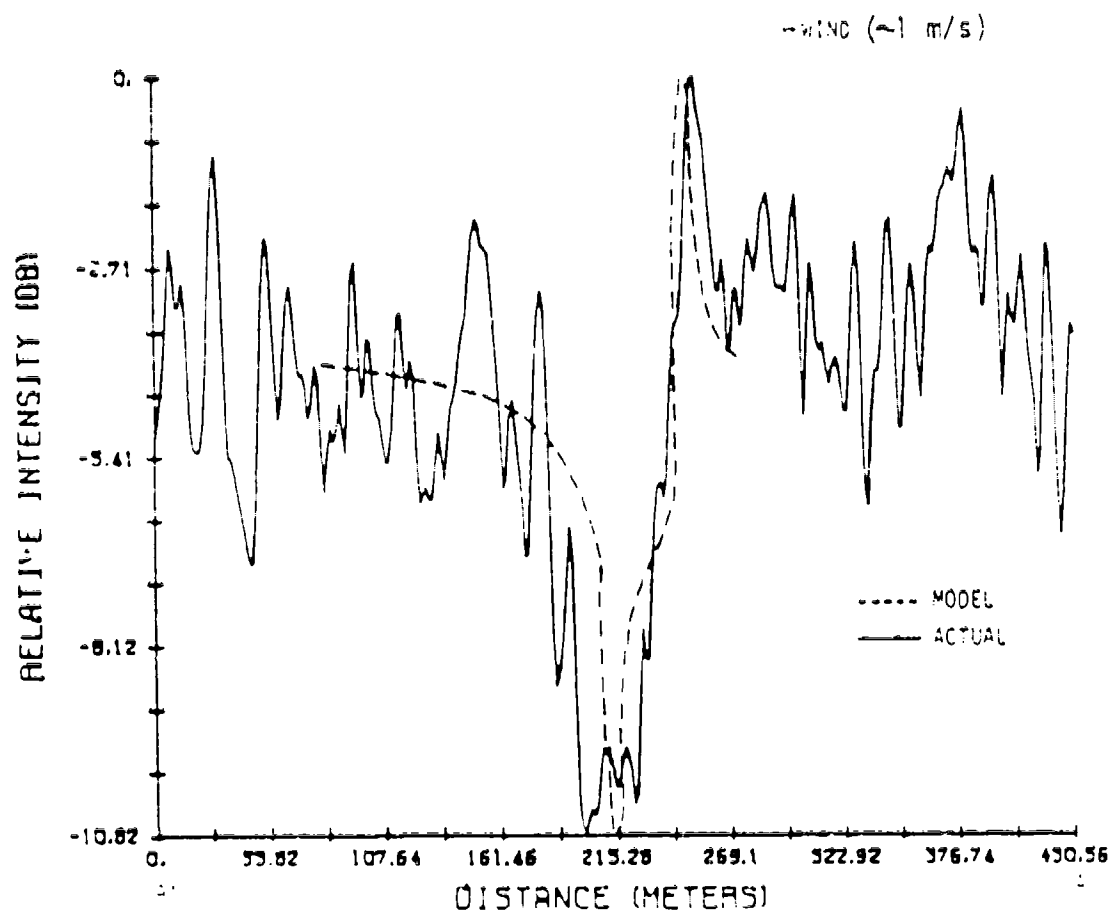


Figure 10. Graphical Comparison of Predicted Radar Backscatter Variation Based on Vortex Model (dashed) and Actual Backscatter Measurements (solid)

achieve the best agreement based on visual observations. The close agreement between the predicted and actual data is obvious.

Some notes of caution should be made regarding these results. The parameters we used in our model were adjusted to match the observed data, however, they were very close to what we would have predicted for the Quapaw. The point we are trying to make in this discussion is that the vortex wake model discussed in the previous section can be used to help explain ship-generated wake features. We use the result discussed above as justification for using this model to predict expected radar signatures for different ship and radar parameters under a variety of wind conditions. This is the topic of the next section.

2.2.2 MODEL PREDICTIONS

One goal of developing the model described above was to be able to predict the detectability of vortex wakes from various ships for a variety of different wavelength radars and surface wind conditions. Predictions of this type would also help define an optimum radar system for vortex wake detection.

Two ship cases were used in our simulations corresponding to Case 1 and Case 3 in Swanson (1984). These correspond to a small five kiloton displacement military ship and a 500 kiloton displacement supertanker. The parameters for each of these two ships are given in Table 1.

The decay characteristics of vortex-generated surface currents with distance aft of the generating ship were calculated by Swanson (1984) for the two ships we modelled and are shown plotted in Figure 11. It is interesting to note from this plot that the rearward axial current, although smaller initially, decays more slowly than the vortex-related lateral currents and eventually is larger in magnitude. Inclusion of axial currents in a more comprehensive modelling effort is one recommendation resulting from this work.

TABLE 1
SUMMARY OF SHIP PARAMETERS USED IN VORTEX SIMULATIONS

	5 Kiloton Ship (Case 1)	500 Kiloton Ship (Case 3)
Velocity	10 m/s	7.5 m/s
Length	100 m	400 m
Beam	10 m	68 m
Draft	5 m	25 m
Displacement	5 Kton	500 Kton

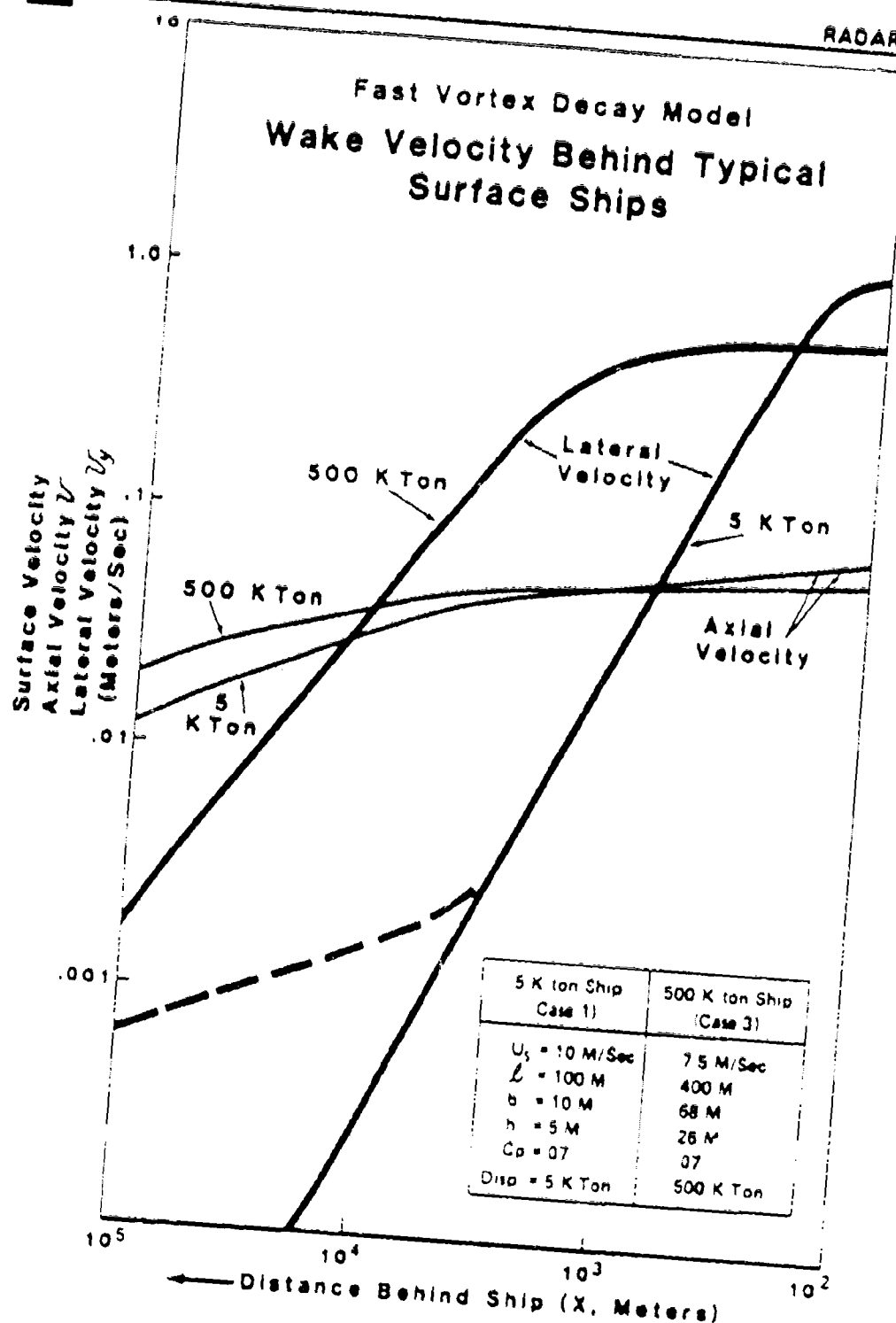


Figure 11. Decay of Wake-Induced Surface Currents as a Function of Distance Behind Generating Ship (from Swanson, 1984)

One set of simulations were generated for the five kiloton ship corresponding to a location one kilometer behind the ship. The peak lateral velocity from Figure 11 is about 3 cm/s. We adjusted the vorticity in our model to produce similar currents. The remaining parameters in our model were fixed at the values predicted by theory. The surface current profile for this case is shown plotted in Figure 12. The detectability of these features as a function of radar wavelength are shown plotted in Figure 13 for wind speeds of 0, 1.5, 3, 6, and 12 m/s. The surface wavelengths we considered included 3.2, 5.7, 25, and 100 cm. At 30° incidence angle, these would correspond to the Bragg wavelengths at X-band, C-band, L-band and 100 cm, respectively.

The parameter we have plotted in Figure 13 is defined as the absolute value of the maximum negative spectral perturbation predicted by our model. This parameter was selected for several reasons. Examination of historic SAR data sets clearly demonstrated that the turbulent wake-like features we feel are related to a vortex mechanism are visible due to a decrease in radar return (negative spectral perturbation) aft of a ship and not due to an increase in radar backscatter along the edges of the wake. Also, our model assumes a saturated Phillips spectrum as the initial unperturbed conditions, it is unclear how this spectrum can be enhanced before the onset of breaking. The detectability of spectral perturbations in SAR imagery is discussed in detail in Appendix A. For our purposes, a spectral perturbation of about 0.15 appears to be the threshold of detectability. This value is indicated on Figure 13 by a dashed line.

The results plotted in Figure 13 show that two effects are occurring. When relaxation effects are not included ($U = 0$ m/s), the shortest waves show the maximum perturbation by the vortex-generated surface currents. When relaxation effects are included, the perturbation of the shorter wavelengths is sharply reduced. This is

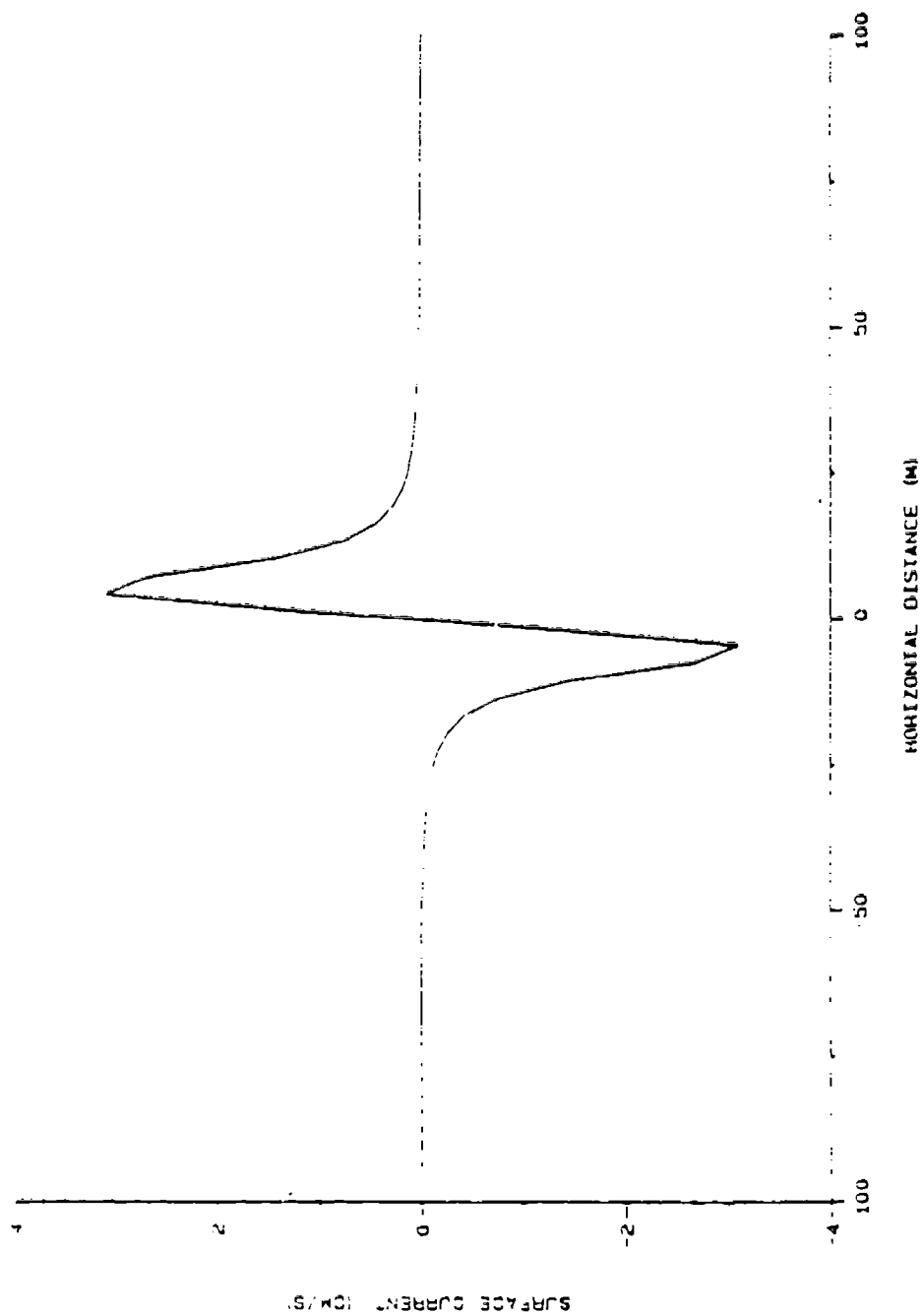


Figure 12. Modelled Vortex-Produced Surface Currents One Kilometer Behind a 5000 ton Ship (Case 1)

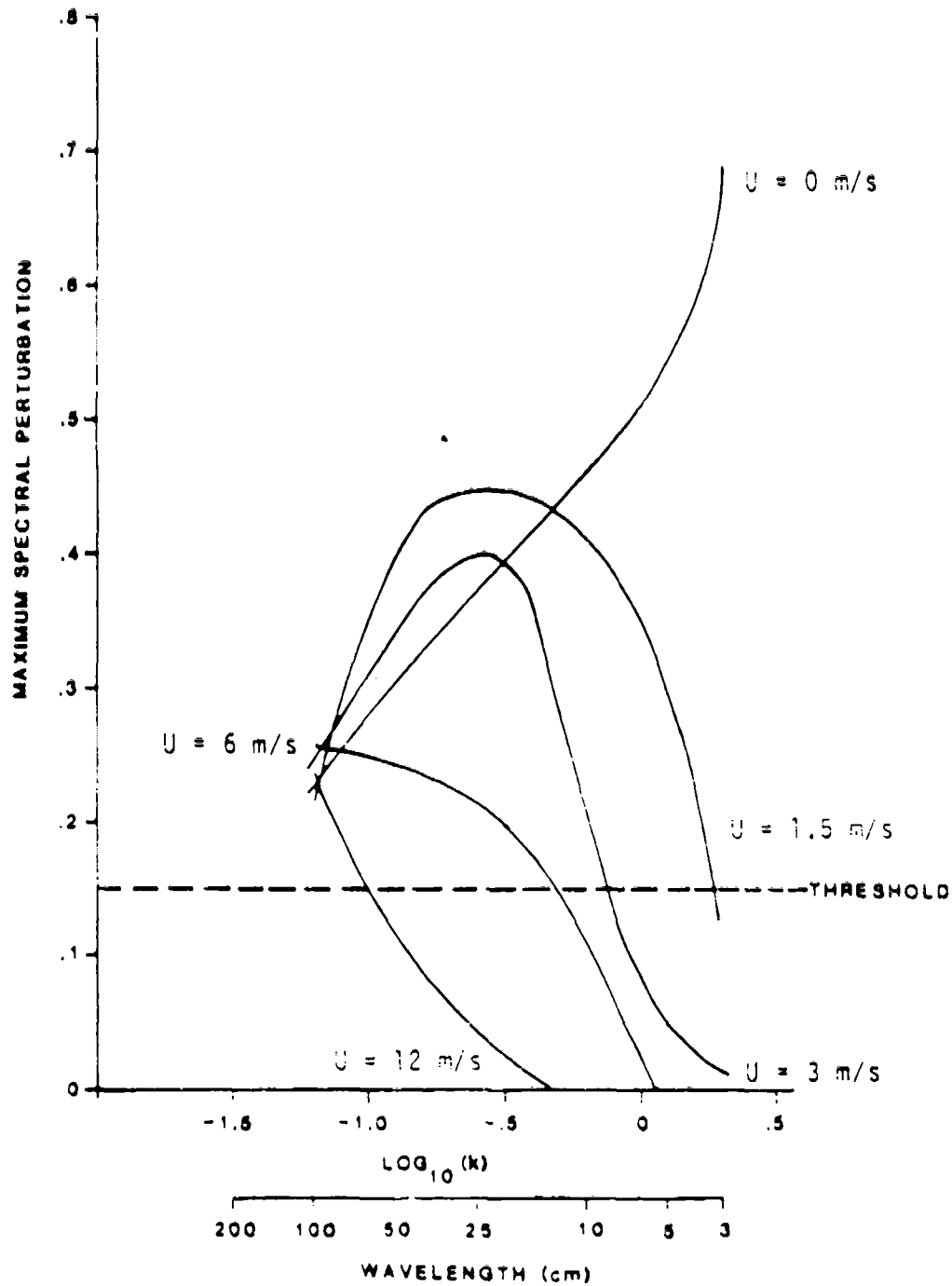


Figure 13. Modelled Detectability of the Vortex-Produced Surface Currents in Figure 11 as a Function of Wavelength and Wind Speed

because waves of these lengths quickly relax back to their equilibrium values. In our model runs, we used a grid spacing of 3 m corresponding to the nominal resolution of existing airborne SAR systems. At longer wavelengths, the perturbations caused by a given current are smaller than for shorter wavelengths, but the relaxation effects are also reduced. This is illustrated in Figure 13 for the 100 cm wavelength case. The perturbation of these waves is smaller than the shorter waves for little or no wind, but it does not change significantly as wind effects are included. One word of caution should be included. Our model assumes a saturated Phillips spectrum; past radar and surface measurements have indicated that this assumption is justified for X- and L-band (3.2 and 25 cm) wavelengths; it has not been demonstrated for 100 cm waves. It should also be noted that the low wind speed simulations may not represent a realistic situation due to the lack of background signal.

A second set of simulations were generated for the 500 kiloton supertanker case corresponding to a location five kilometers behind the ship (Case 3). The peak lateral current velocity for this case is about 12 cm/s as shown on Figure 11. We again adjusted the vorticity in our model to produce similar currents. The remaining parameters were fixed at values predicted by theory. The surface current profile calculated for this case is shown plotted in Figure 14. The maximum spectral perturbations caused by this current field is shown in Figure 15 as a function of surface wavelength and wind speed. Due to the large currents associated with this case, our model could not be used for the zero wind case or for the two shorter wavelength examples. However, the cases which were run illustrate the important points.

Similar to the Case 1 study presented above, the spectral perturbations caused by the vortex-related currents is a maximum at shorter wavelengths for very low wind speeds and at longer wavelengths for higher wind speeds. In contrast to the Case 1 results

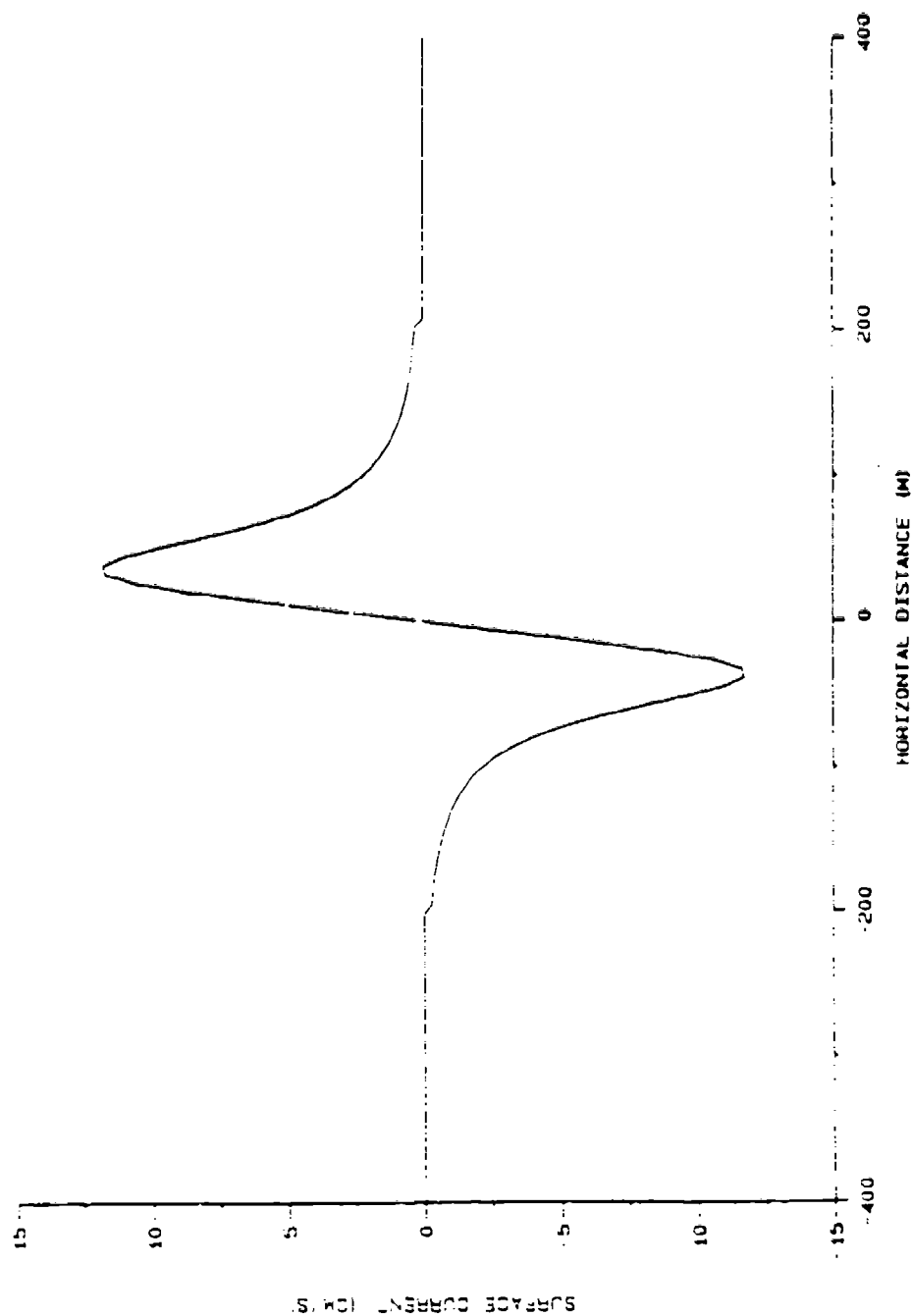


Figure 14. Modelled Vortex-Produced Surface Currents Five Kilometers Behind a 500 Kiloton Ship (Case 3)

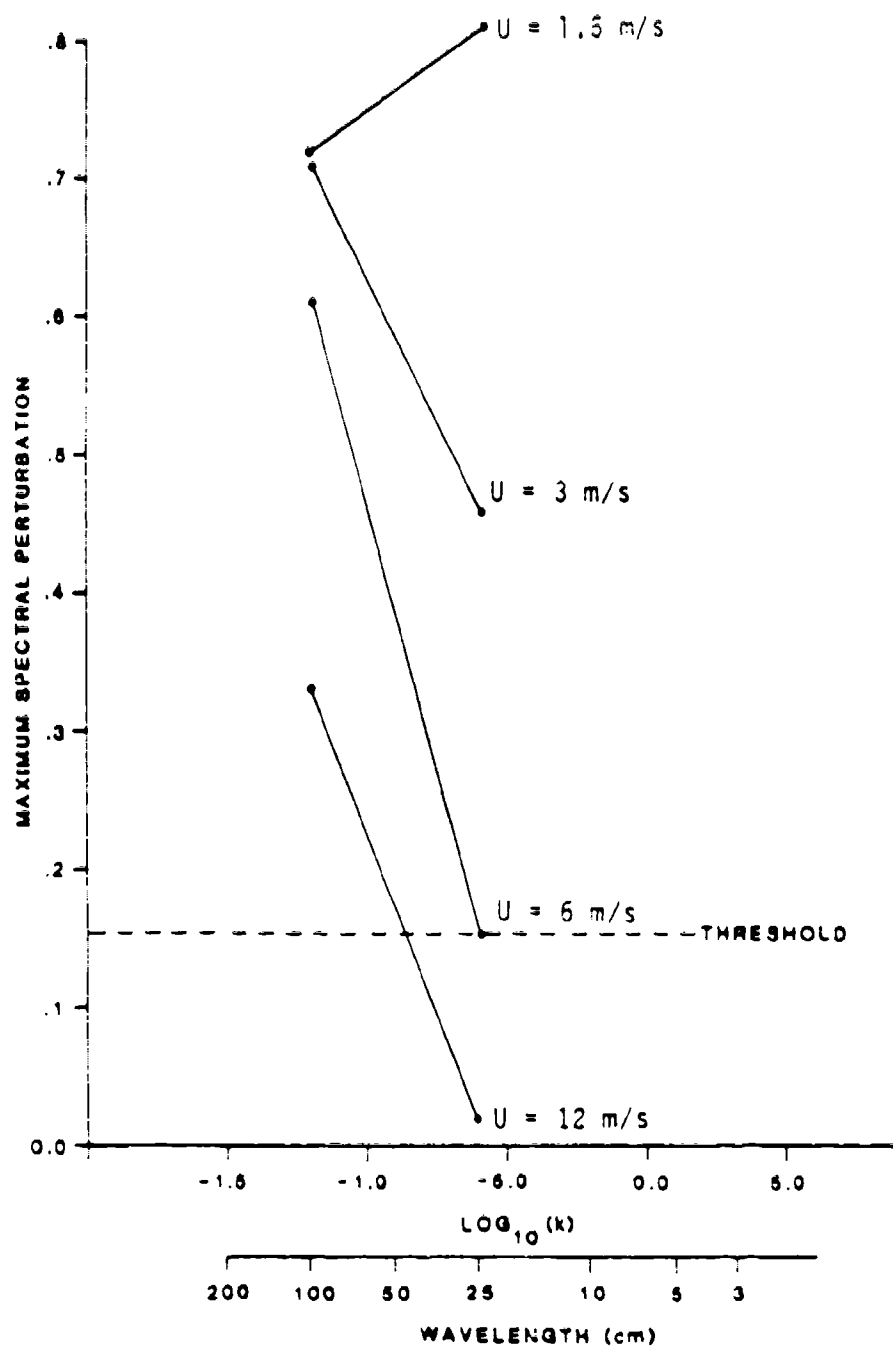


Figure 15. Perturbations Caused by the Vortex-Produced Surface Currents in Figure 14 as a Function of Wavelength and Wind Speed

presented in Figure 13, the negative perturbation of 100 cm waves is very high for low wind speeds but decreases fairly rapidly as the wind increases. Recall that for Case 1, the spectral perturbation of the 100 cm waves remained nearly constant for the wind speeds considered. It is also interesting to note that the perturbation of the 25 cm waves for this case is greater than the Case 1 perturbations at 1.5 and 3 m/s wind speeds, but less than the Case 1 perturbations for 6 and 12 m/s winds. These results can be explained within the context of our model.

At very low wind speeds, the spectral perturbation of surface waves is proportional to the surface current velocity. At very high wind speeds, the spectral perturbation is proportional to the strain rate (du/dy), which is the spatial derivative of the surface current profile. At intermediate wind speeds, the spectral perturbation is proportional to some combination of current and strain rate effects. The wind speed at which the strain rate becomes important depends on the surface wavelength being considered and occurs at a lower wind speed for short waves. In the observations above, the surface currents in Figure 12 were only about one-third as large as those in Figure 14, but the strain rates were about twice as large. The fact that the perturbation of the 100 cm waves in the Case 1 simulation remain nearly constant indicates that the relative magnitude of the current and strain rate effects are approximately equal. The decrease in spectral perturbation of the 100 cm waves for Case 3 as the wind speeds increase indicates that the strain rate contribution is becoming important. Finally, the fact that the perturbation of the 25 cm waves is greater in the Case 1 study for wind speeds of 6 and 12 m/s, even though the surface currents were smaller, clearly indicates that for this wavelength and those wind speeds, the strain rate is the dominant factor.

A third and final set of simulations were generated for the 500 kiloton supertanker case (Case 3) corresponding to a location ten

kilometers behind the ship. The peak lateral current velocity for this case is about 4.5 cm/s as shown on Figure 11. The vorticity in our model was adjusted to match these currents. The remaining parameters were consistent with the previous set of simulations. The surface current profile for this case is shown plotted in Figure 16. The spectral perturbations caused by these current fields is shown in Figure 17 as a function of wavelength and wind speed. These results are what we would expect based on the discussion above. Both the surface currents and strain rates are only about one-third of their values in the previous set of simulations. This reduces the spectral perturbations at both low and high wind speeds.

A final plot was produced which illustrates the spectral perturbations caused by vortex-related wakes as a function of distance aft of the generating ship. This plot is shown as Figure 18 and was generated from the Case 3 simulations discussed above. These perturbations correspond to locations 5 and 10 km behind a supertanker and are plotted for 25 and 100 cm wavelengths and wind speeds ranging from 1.5 to 12 m/s. These results indicate that the spectral perturbations significantly decrease due to the decay of the vortex-generated surface currents. These results indicate that 25 cm surface waves would not be detectable at either location under 12 m/s winds. At 10 km behind the ship, the 25 cm waves would not be detectable with 6 or 12 m/s winds and only marginally detectable for 3 m/s. The 100 cm surface waves would only be marginally detected at the 10 km position for 12 m/s winds.

The simulations presented above have indicated several things. At very low wind speeds, the spectral perturbations associated with ship-generated vortices are a maximum for shorter wavelengths. As wind speed increases, wave growth or relaxation effects cause the perturbation of the shorter waves to decrease sharply. Although they are not as strongly perturbed for a given current pattern at low wind speeds, longer surface waves are more insensitive to relaxation

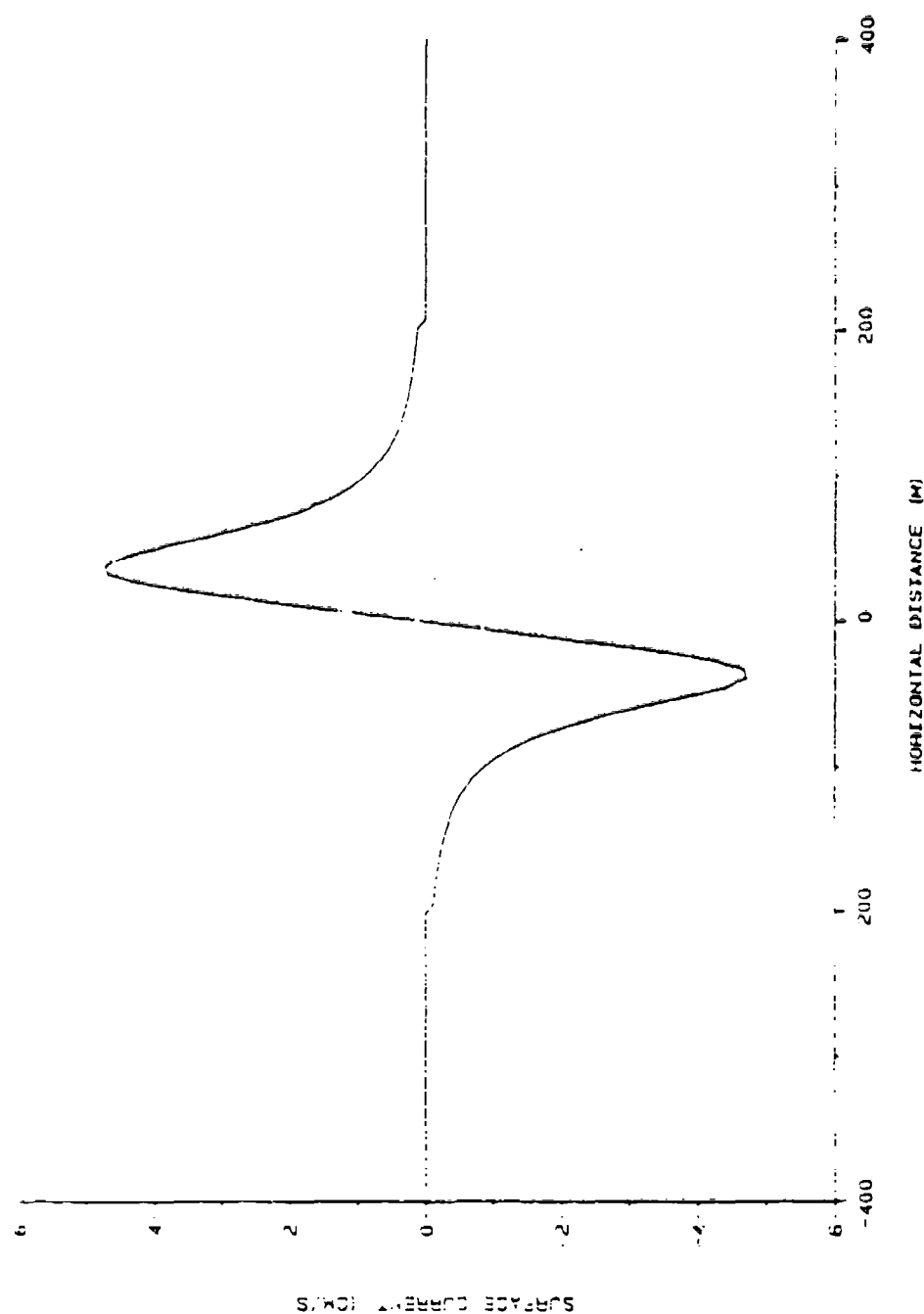


Figure 16. Modelled Vortex-Produced Surface Currents ten Kilometers Behind a 500 Kiloton Ship (Case 3)

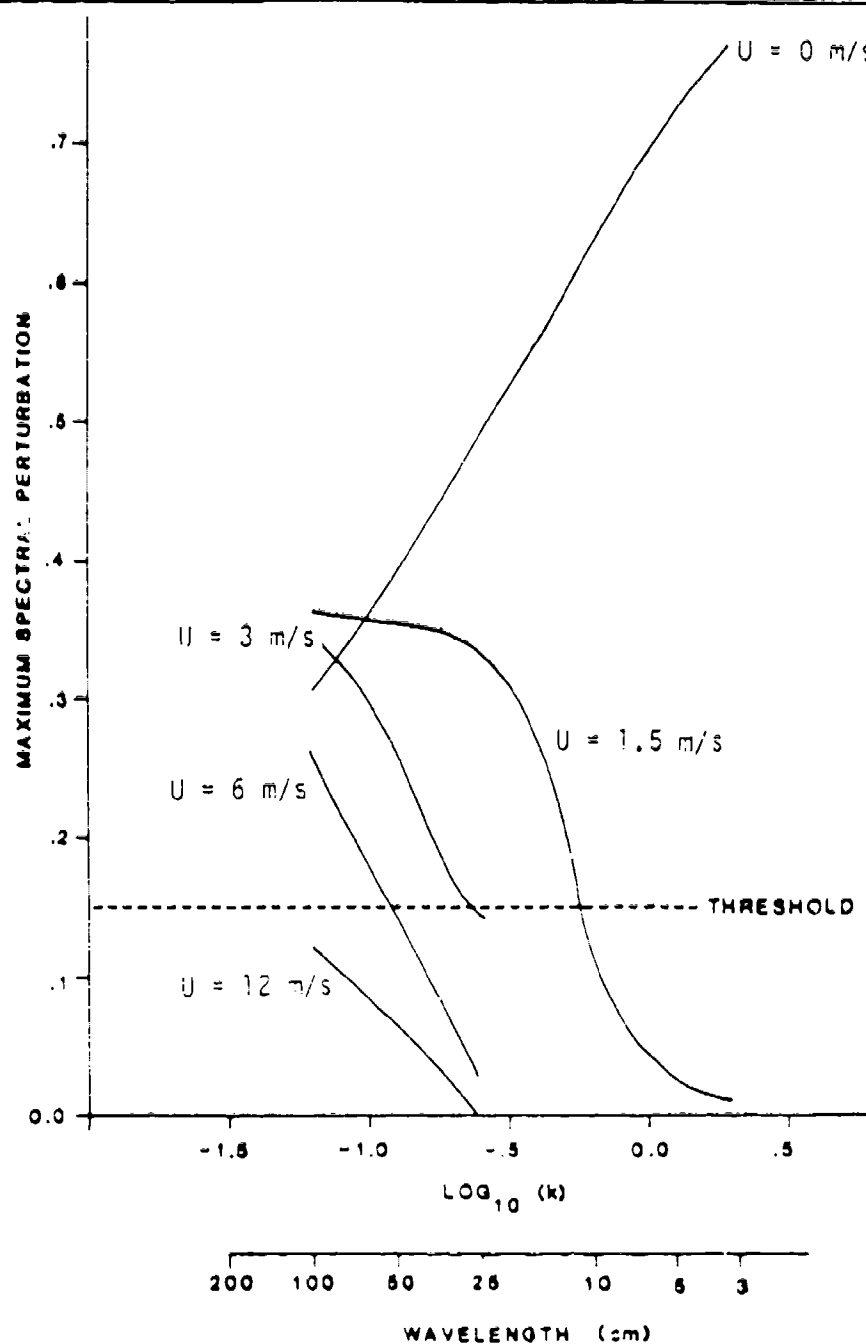


Figure 17. Modelled Perturbations of the Vortex-Produced Surface Currents in Figure 16 as a Function of Wavelength and Wind Speed

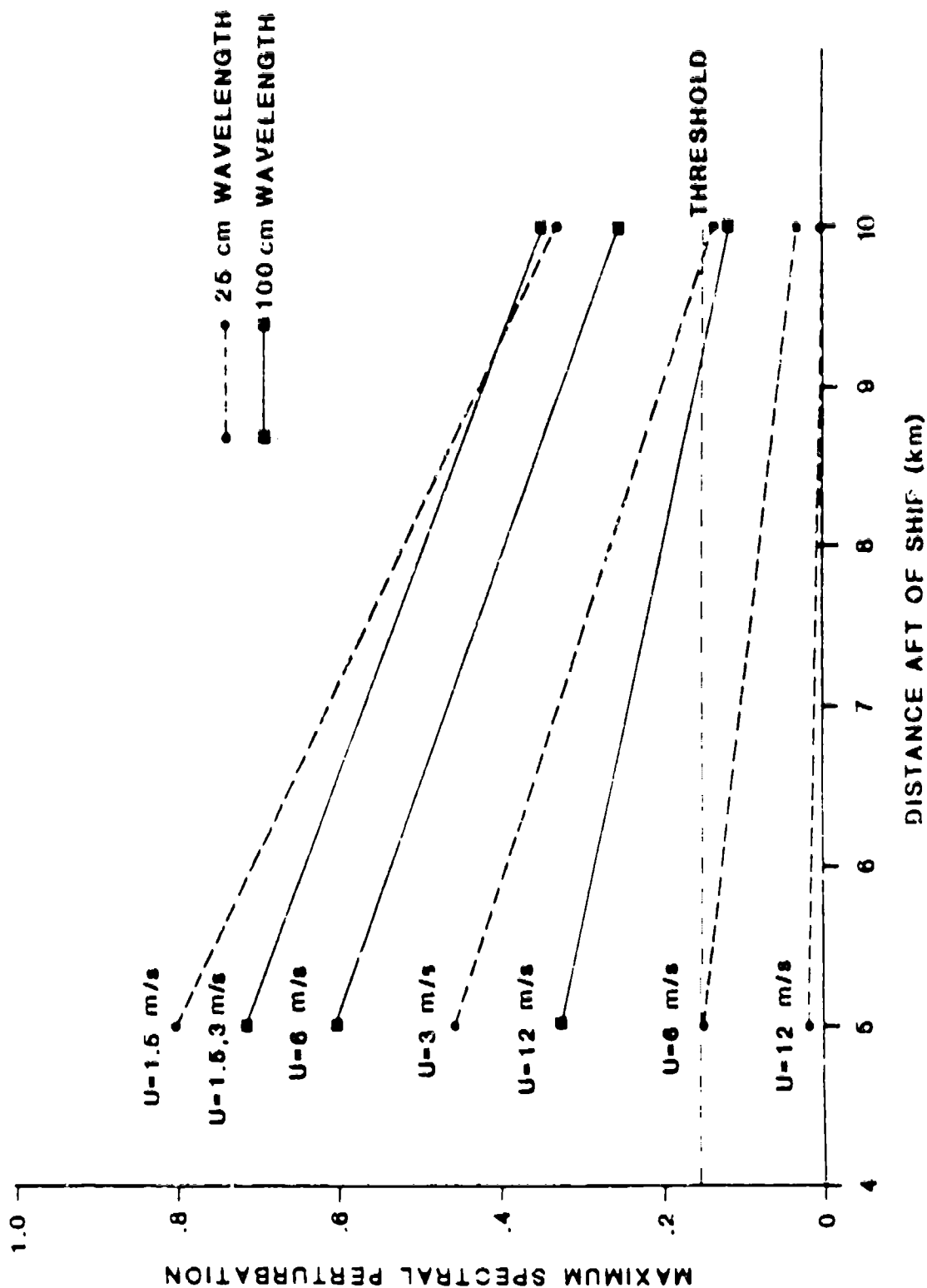


Figure 18. Modelled Perturbations of Vortex-Produced Makes for Case 3 as a Function of Wavelength, Wind Speed, and Distance Aft of the Ship

effects and offer the possibility of detection at higher wind speeds. Ideally, one would want a sensor which would be sensitive to the short waves under low winds, and longer waves for higher wind speeds. One possibility would be a multiple frequency SAR system.

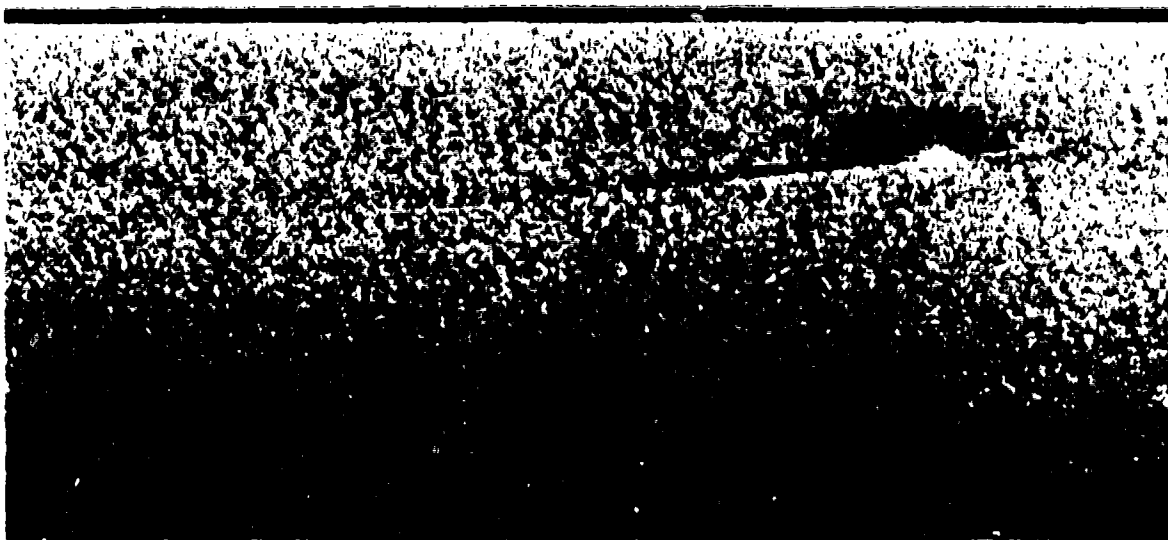
The results of our simulations also indicate that the type of ship generating the vorticies also determines their detectability. At low wind speeds, the spectral perturbation of surface waves is proportional to surface currents, which in our model are proportional to ship velocity and beam and inversely proportional to the square root of the length. At higher wind speeds, the spectral perturbation is related to the strain rate. The strain rates would be highest for those cases where the vorticies shed by the ship have not spread apart significantly. This would be true for narrow ships with high velocities.

The reader should be cautioned that the model we have used above is only a first-order approach to the problem. The effects of the rearward axial current should be included as part of extending the model to two dimensions. We would also like to include SAR imaging considerations into the model such as motion effects, scatterer coherence time, and variable resolution.

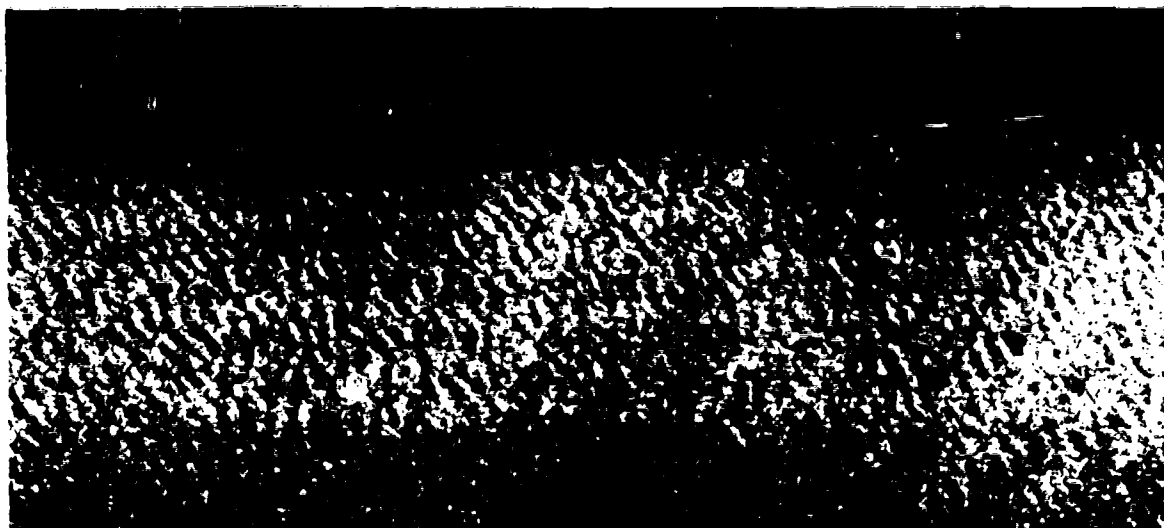
2.3 ADDITIONAL IMAGERY

Presented below are several SAR images of ships and what appear to be turbulent wake features. Very little is known about the ship parameters in these images or the surface wind conditions during the data collections. This limits our discussions of these images to a general qualitative nature.

Figure 19 represents simultaneously collected L- and X-band SAR imagery of a ship towing a barge. In each image, a turbulent wake feature is observed aft of the barge. In the L-band image, the wake feature is observed to have a bright edge and a band of reduced



L-Band



X-Band

1 km

Figure 19. L- and X-Band Optical SAR Imagery of a Turbulent Wake Feature Collected 2 November 1978

backscatter which gradually returns to the background intensity about 5 km aft of the barge. In the X-band image, a narrow bright arm is observed and also a very narrow dark return area extending to about 4 km behind the ship. We believe that the wind direction for these data was towards the top of the page. This is based on the bright arms observed in the imagery where we feel the vortex-induced currents and wind-generated capillary waves are in opposition. We made a rough attempt at modelling these features by assuming a current pattern of the same form as Case 1 in the previous section. In our model runs, we assumed a wind speed of only 1 m/s. The surface current profile and spectral perturbations predicted by our model are shown in Figure 20 for the L-band Bragg waves. The modelled spectral perturbations qualitatively agree with the image observations, that is, a narrow line of increased backscatter on the assumed upwind side of the wake and a broader region of decreased backscatter downwind. The modelled perturbations for the X-band Bragg waves are presented in Figure 21. These results do not agree as well with the imagery as the L-band, but nevertheless, several points can be made. The model does not predict the bright narrow arm on the assumed upwind side of the wake which is observed in the data. We do not fully understand this but think that the SAR may be sensing short waves created by the breaking of longer waves. The model does predict the narrow line of decreased backscatter observed in the imagery. The structure of the modelled perturbations in Figure 21 indicates that there may be cases where two lines of decreased backscatter extend behind a ship with the water between them having relaxed back to equilibrium. This has in fact been observed in numerous cases and is referred to as turbulent wake splitting. An example is shown in Figure 22.

A Seasat SAR image of a ship in the Gulf of Alaska is shown in Figure 23. This particular image is from Fu and Holt (1982), and they speculate that the ship is an oil tanker with a visible turbulent wake up to 12 km behind the ship. Wind speeds of about 7 m/s

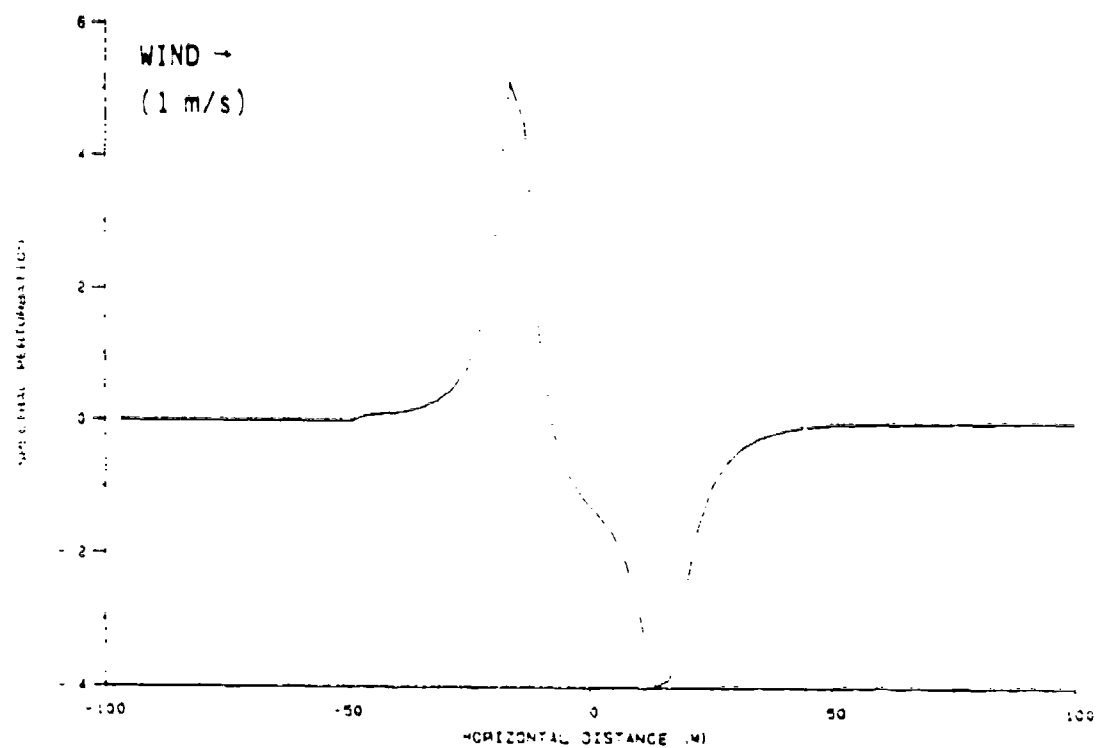
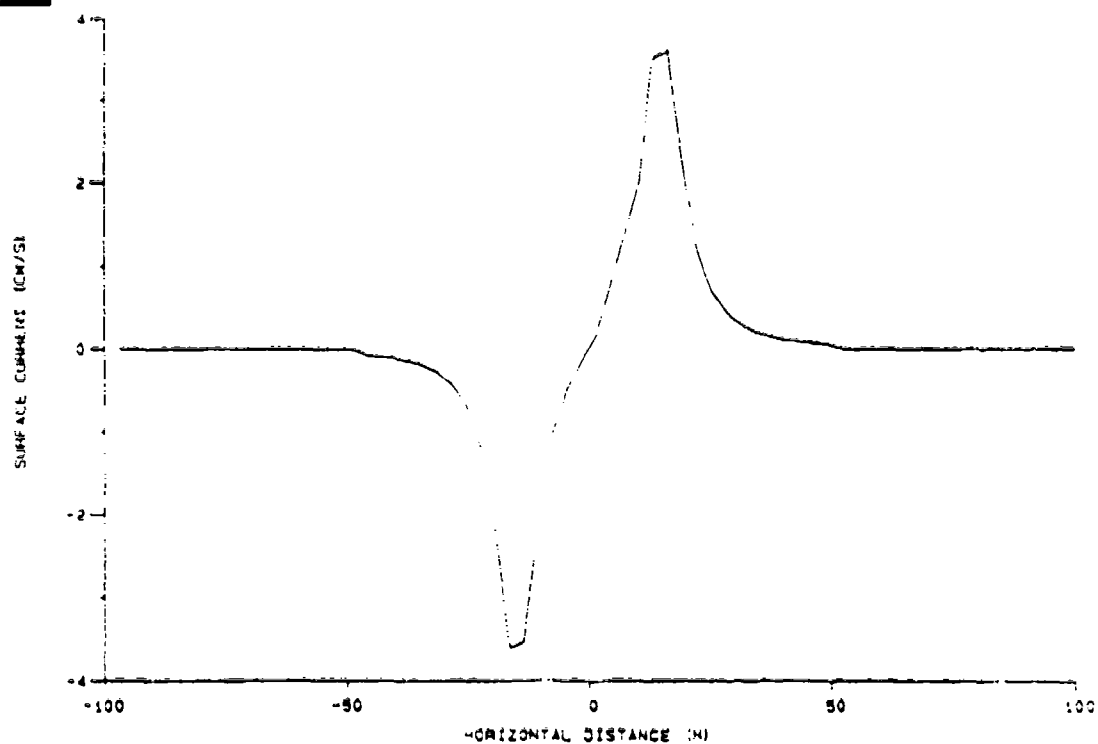


Figure 20. Estimated Surface Current Profile and Modelled Spectral Perturbations for L-Band Bragg Waves Corresponding to Figure 19

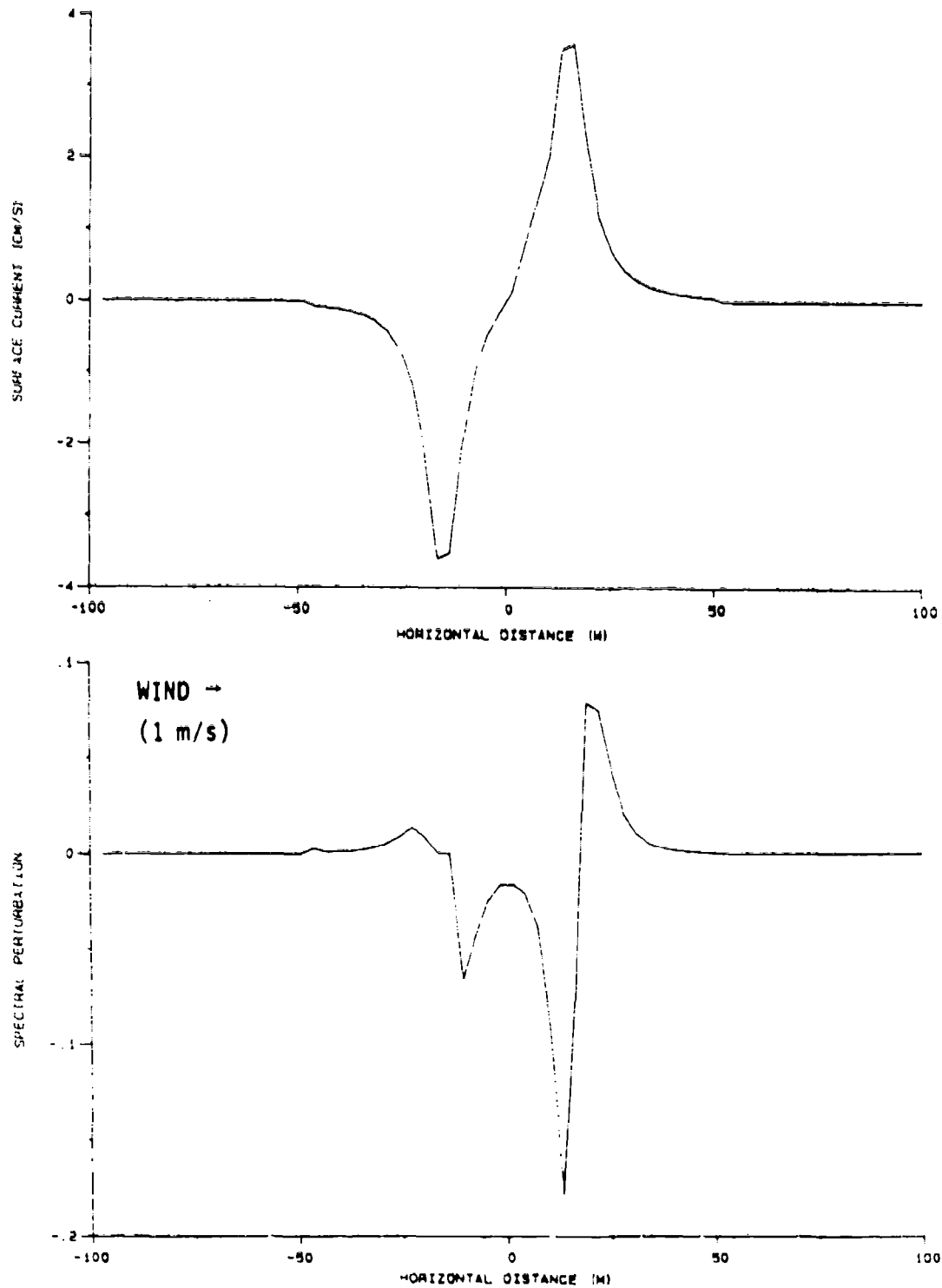


Figure 21. Estimated Surface Current Profile and Modelled Spectral Perturbations for X-Band Bragg Waves Corresponding to Figure 19

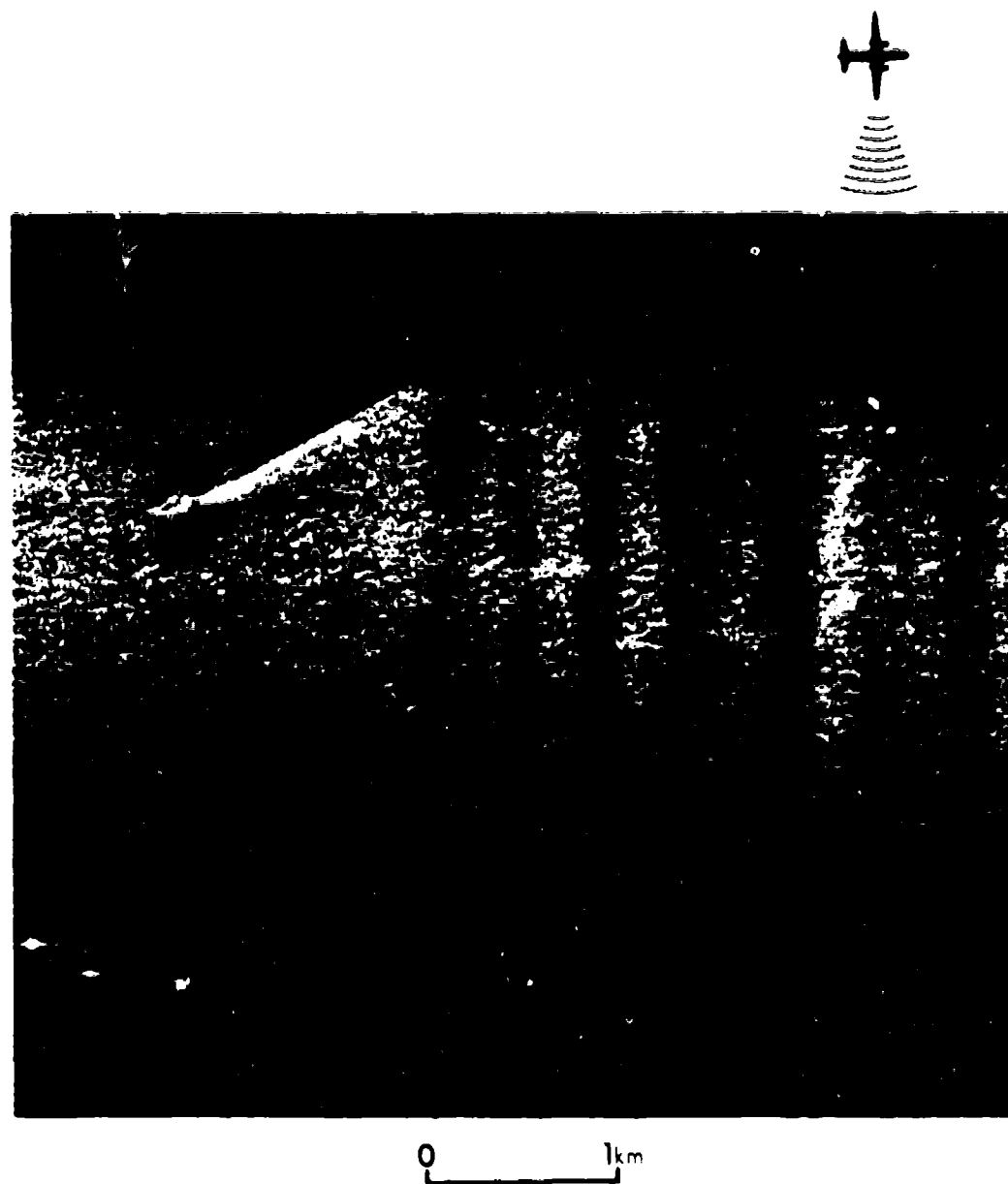


Figure 22. X-Band Optical SAR Image Indicating Turbulent Wake Splitting (Pass 2, 3 November 1978)

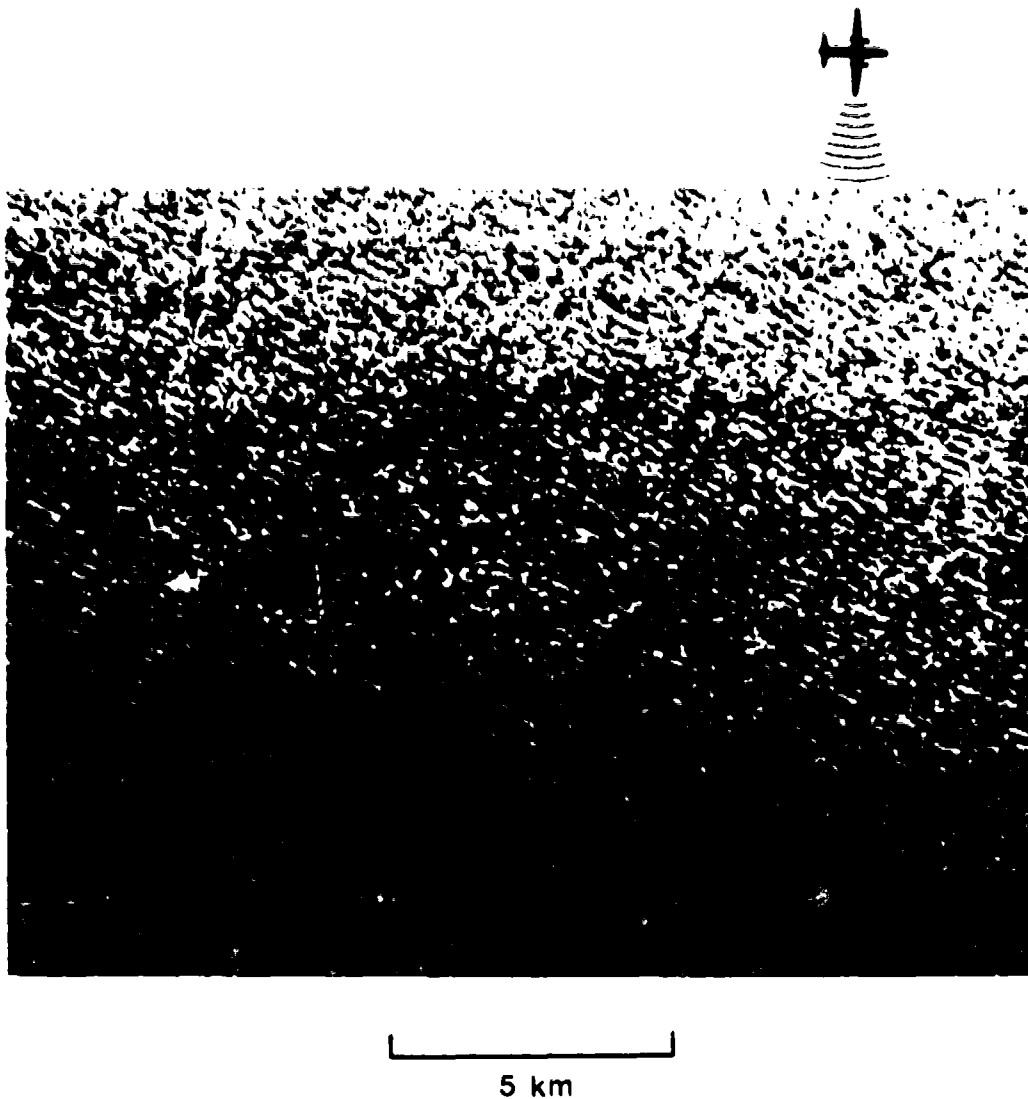


Figure 23. Seasat SAR Image of Suspected Oil Tanker in the Gulf of Alaska (after Fu and Holt, 1982)

were measured during this data collection. Using the Case 3 current profile corresponding to 10 km behind the ship, a peak spectral perturbation of 0.06 is found for these wind conditions. Earlier, we qualitatively determined that a spectral perturbation of 0.15 ± 0.05 was necessary for detection of a wake feature in SAR imagery. Recall that Seasat SAR data was typically processed to four looks; this reduces our detectability requirements to about 0.075 ± 0.025 so our model results appear consistent with the image observations.

Two X-band SAR images of ships and their wakes are presented in Figure 24. These images are both from the same pass of data separated by about 20 km. The wind speeds during the collection of these data was very low, in fact, visual observations during these flights indicated that the ships were the only source of surface roughness. The ship in Figure 24(a) is displaced from its wake due to its range velocity component. The speed of this ship has been estimated from this displacement at about 10 m/s. The radar return behind this ship is concentrated into two narrow lines extending aft of the ship. In Figure 24(b), the radar return behind the ships consists of a region of slightly increased backscatter. The Doppler displacement of these ships indicated speeds of about 6 m/s. Recall from Section 2.1 that the magnitude of surface currents associated with ship-generated vortices is directly proportional to ship speed. We feel that the higher speed of the ship in Figure 24(a) is creating higher surface currents which concentrate the ship-generated roughness along two narrow lines corresponding to the vortex locations.

Our final example is an X-band optical image of a large ship in the Norwegian Sea presented as Figure 25. We have estimated the wind speeds as 10 m/s during the data collection. Observed on the image are the two arms of the Kelvin wake and two bright narrow lines extending behind the ship. At these wind speeds, the perturbation of X-band Bragg waves due to wave-current interactions is close to zero. One possibility is that the wake features in this image are due to the generation of Bragg-scale waves by the breaking of longer waves.



(a)

1 km



(b)

Figure 24. X-Band Optical SAR Imagery Collected During Very Low Wind Conditions of (a) a Relatively Fast Moving Ship, and (b) Slow Moving Ships

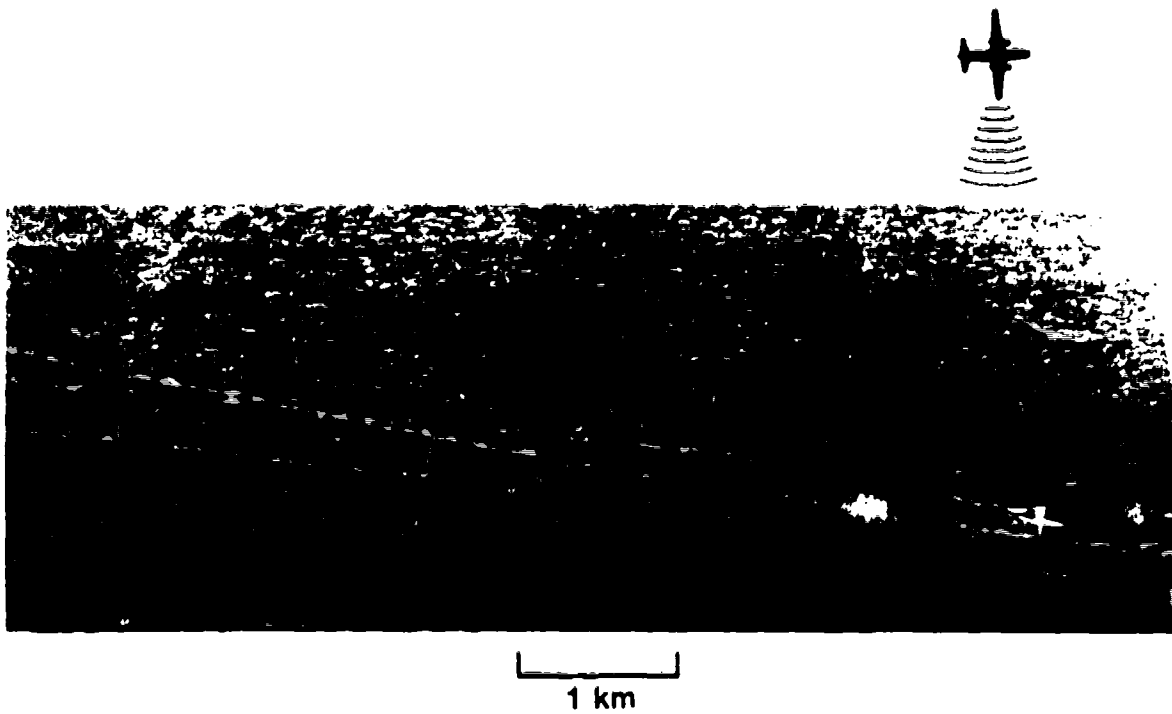


Figure 25. X-Band Optical SAR Image Indicating Wave Breaking
Due to Vortex Current Interactions

2.4 RESOLUTION EFFECTS

In addition to the radar wavelength dependence of SAR ship wake detection, the resolution of the SAR system being considered will also determine what ship wake components will be detected and to what degree. To study the effects of changing resolution, a digital L-band ship wake image collected during the 1983 Georgia Strait Experiment was reprocessed with a reduced bandwidth corresponding to Seasat parameters. The original full bandwidth image is shown in Figure 26(a). This image has a resolution of about 4 m in both slant range and azimuth. Visible in the image are the turbulent wake, stern waves, and both arms of the Kelvin envelope. For a general discussion of these various components refer to Lyden et al. (1985a). This image was reprocessed with reduced bandwidths corresponding to one-look Seasat resolutions of 8 x 7 m in slant range and azimuth, respectively, and is presented as Figure 26(b). At these reduced resolutions, only the turbulent wake is visible, and its detectability has dropped relative to the full resolution image.

A comparison of actual Seasat imagery with simultaneously-collected aircraft data of a ship wake is shown in Figure 27. These data were collected in the Georgia Strait in 1978. Stern waves are faintly visible in the aircraft data as well as a clearly defined turbulent wake. Only a very faint turbulent wake is visible in the Seasat data. A comparison of these data with the aircraft and aircraft-simulated Seasat data in Figure 26 reveals several things. In both cases, stern waves were visible in the aircraft data but not in the Seasat case. Turbulent wakes are also clearly visible in the aircraft data, but are not as clearly visible in the Seasat or Seasat-simulated data. This comparison clearly illustrates the effects of resolution on the detectability of subtle patterns, and also shows that these effects can be simulated by appropriate processing of high resolution aircraft data.



250 m

(a) L-BAND DIGITAL AIRCRAFT DATA



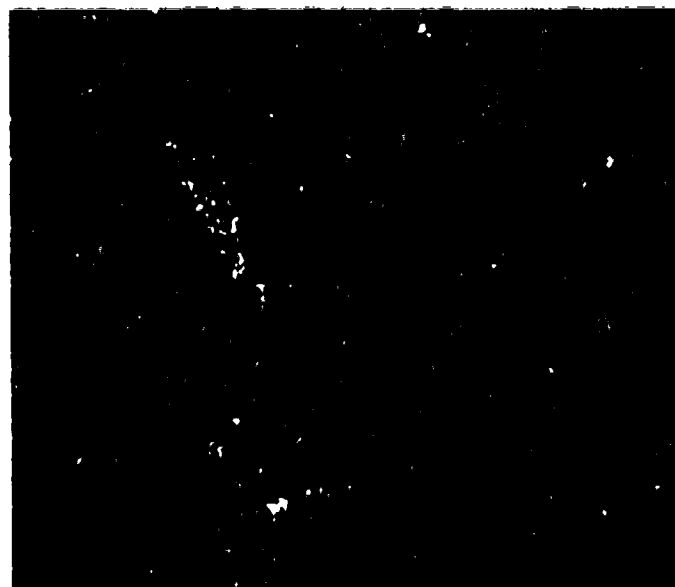
(b) SEASAT-SIMULATED DATA

Figure 26. L-Band Digital Aircraft SAR Data Processed to
(a) Full Resolution, and (b) Simulated Seasat
Resolutions



(a) L-Band Aircraft Data

1 km



(b) Seasat Rev 474

1 km

Figure 27. Coincident L-Band SAR Imagery Collected by
(a) Aircraft, and (b) Seasat

The ability to simulate satellite ship wake SAR imagery using existing aircraft data is important for several reasons. Simulations of this type can be used to determine resolution requirements for the detection of various ship wake components. An example, would be to determine the resolution necessary to detect the stern (transverse) waves visible in Figure 26(a). This could be accomplished by repeatedly processing this data at coarser resolutions until the stern waves disappear. These simulations can also be used to predict the ship wake signatures which can be expected from future satellite systems.

2.5 DETECTION APPLICATIONS

The final study we performed as part of our ship wake analysis was to examine the Fourier transform of a ship wake image for unique characteristics which could then be used in an automated detection algorithm. The ship wake data we used in this study was collected during the 1983 Georgia Strait Experiment and is presented in Figure 28. The wake feature in this image is composed of two bright narrow arms which are modulated by the stern waves. This image was fast Fourier transformed and the resulting spectrum is displayed in Figure 29. These results are displayed in wavenumber space so that the center of this image corresponds to zero frequency or DC, with increasing distance from this point representing shorter wavelengths. The horizontal and vertical scales on Figure 29 are different because we transformed a rectangular rather than a square region. Several features are visible in the transform. Two lines of low-frequency energy are present corresponding to and aligned perpendicular to the narrow arms in the ship wake image. These are what would be expected if the arms in the image could be modelled as solid lines. The spectral resolution of this transform allows these arms to be differentiated. There is also a well-defined spectral component which is nearly vertically-aligned with a wavelength of about 35 m. This

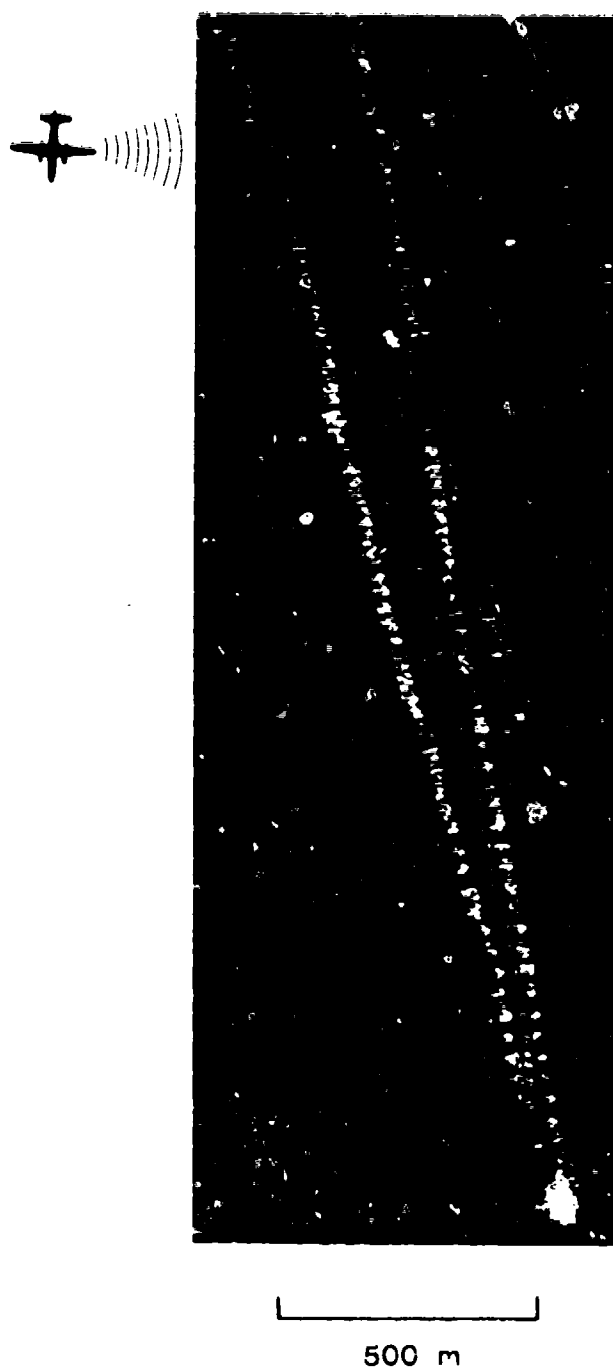


Figure 28. L-Band Ship Wake Image Used in Detection Studies

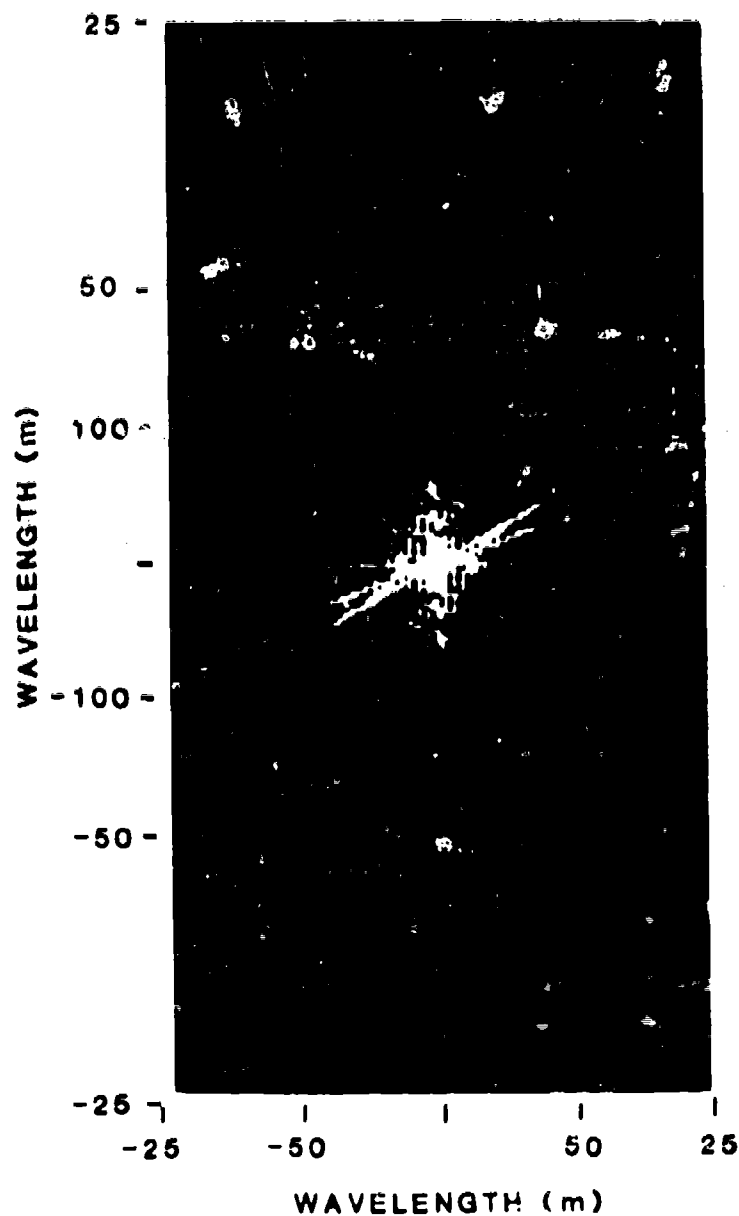


Figure 29. Fast Fourier Transform Magnitude Spectrum of SAR Image Shown in Figure 28

is the modulation we have associated with the 35 m wavelength stern waves. These waves travel at the same velocity as the ship generating them, thus, they are very monochromatic for a constant velocity ship. With some pre-filtering, to remove noise effects, this component could be enhanced. Since monochromatic waves at lengths of 30-60 m are not expected in the open ocean, this component being present in Fourier transformed SAR data may indicate ship-generated stern waves.

A subset of the ship wake image discussed above is shown in Figure 30. This subset was extracted from the image shown as Figure 27 and its Fast Fourier Transform (FFT) was calculated. The spectrum of this transform is presented in Figure 31. Several interesting features are present in this spectrum. The wake arms are not resolved as they were in Figure 29. This is because spectral resolution is degraded as the area being transformed is decreased. Again, there is a significant component at about 40 m wavelength which is associated with the stern waves.

The work described above is very preliminary in nature. Additional work in this area would include modelling the expected transforms of ship wake features, and seeing how the modelled results compare with transforms of natural phenomena. This would provide insight into the uniqueness of the ship wake features. Other techniques besides the Fourier transform should also be investigated for automated detection applications.

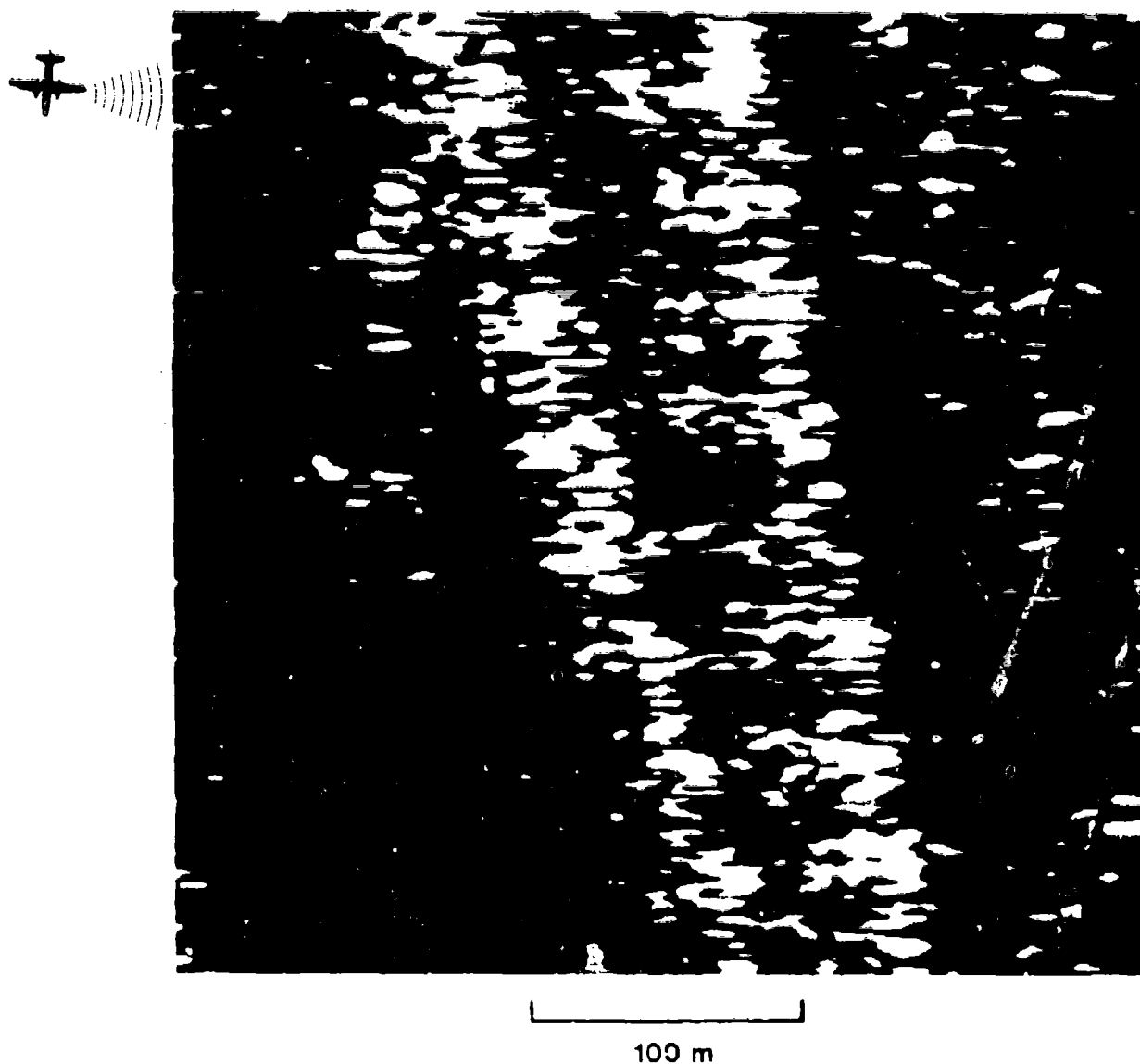


Figure 30. Subset of Ship Wake Image Shown in Figure 28 Used in Detection Studies

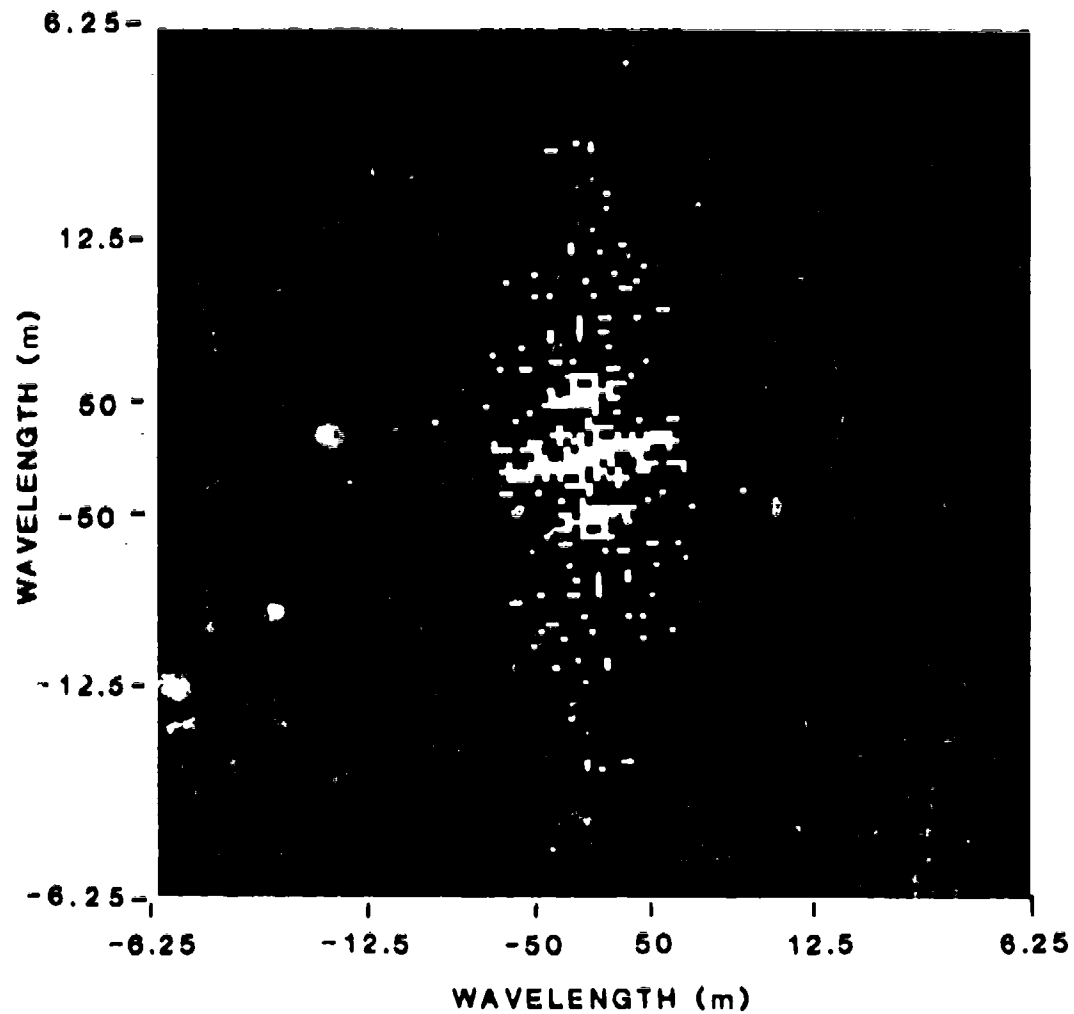


Figure 31. Fast Fourier Transform Magnitude Spectrum of SAR Image Shown in Figure 30

3

CONCLUSIONS AND RECOMMENDATIONS

The primary purpose of this investigation was to study the dark wakes observed in SAR imagery behind moving ships. A first attempt has been made at using a hydrodynamic model for surface currents associated with ship-generated vortices as input into a wave-current interaction model which predicts a spectral perturbation of the wavelength under consideration. These simulations were performed at wavelengths corresponding to the Bragg waves for various radars. Spectral perturbations of their Bragg waves are what radars are sensitive to. For the cases considered, the simulated wake signatures generally agreed to those observed in the actual data. Our results indicate several things.

The spectral perturbations associated with a vortex-related surface current pattern are larger at shorter wavelengths than at longer wavelengths. Therefore, at low wind speeds where wind effects are negligible, a vortex-related surface current pattern would be most detectable by a radar which was sensitive to shorter waves. In higher wind conditions, the shorter wavelengths regenerate more quickly than the longer wavelengths. Therefore, although the vortex-related surface currents have a greater effect on the shorter waves, these waves quickly return to saturation. This return to equilibrium occurs over a fraction of a typical SAR resolution cell thereby masking any current-related features in the imagery. Although longer surface waves are not as sensitive to surface currents, they regenerate more slowly in response to wind. Therefore, at higher wind speeds, a vortex-related surface current pattern would be most detectable by a radar which was sensitive to longer waves. Ideally, one would want a radar which would be sensitive to the short waves under low winds, and longer waves for higher wind speeds. One possibility would be a multiple frequency SAR system.

The results of our simulations also indicate that the type of ship generating the vortices determines their detectability. At low wind speeds, the spectral perturbation of surface waves is proportional to surface currents, which in our model are proportional to ship velocity and beam and inversely proportional to the square root of the length. At higher wind speeds, the spectral perturbation is related to the strain rate which is the spatial derivative of the surface current profile. Strain rates would be highest for those cases where the vortices shed by the ship have not spread apart significantly. This would be true for narrow ships with high velocities.

Recommendations for future work in this area would be to include the rearward axial current into our model and to extend this model to perform two-dimensional simulations. This rearward current is initially smaller than the vortex-related lateral currents, but decays more slowly with time. We would also like to include the effects of coherence time, scatterer motion, and variable resolution in our model.

Other analyses which were performed as part of this study included examining the relationship between SAR resolution and the visibility of various ship wake components. This was done by processing aircraft SAR data of a ship wake with a reduced bandwidth corresponding to the Seasat SAR. A comparison of the two processings indicated that many of the ship wake components were lost at the coarser resolutions. A comparison of simultaneously collected aircraft and Seasat SAR data indicated that our Seasat simulation produced reasonable results. Using existing aircraft data, we can use this approach to predict what ship wake features future satellite SARs should be able to detect as well as help to define resolution requirements for future SAR design.

The final part of this study examined the Fourier transform of SAR ship wake imagery for unique information which could be used in automated detection algorithms. Results of this study were inconclusive but indicated that there is some information in the ship wake image transform which may be unique and be able to be used for detection purposes. Recommendations for future research include modelling observed ship wake signatures and their transforms and comparing these to targets which would be expected to occur naturally.

APPENDIX A SAR DETECTABILITY OF SURFACE WAVE PERTURBATIONS

The detectability of vortex wake-induced current patterns by SAR depends not only on the spectral perturbation of the Bragg wavelengths caused by the currents, but also on the size of the perturbed region and the resolution and speckle characteristics of the SAR system. Presented below is a brief discussion on how these various factors influence the detectability of vortex-related patterns in SAR imagery. Several image simulations are presented which help illustrate these effects.

The model we have employed in our vortex wake simulations calculates the spectral perturbation at a specified wavelength due to interactions with vortex-induced surface currents (see Section 2.1). Spectral perturbations of the Bragg wavelengths are assumed to be directly proportional to changes in radar backscatter. The detectability of these backscatter changes in a SAR image is dependent on the magnitude of the spectral perturbation, the extent of the perturbed region relative to the SAR resolution, and the speckle characteristics of the SAR system.

Simulated SAR images were produced for the spectral perturbation pattern shown in Figure A-1. This pattern consists of different width lines with spectral perturbations ranging from 0.0 on the extreme left of the pattern to 0.5 on the extreme right side. The vertical width of these features ranges from two pixels at the top of the pattern to 16 pixels at the bottom. Intuitively, the detectability of these features should increase with size and spectral perturbation.

The simulated SAR image presented in Figure A-2 was generated assuming a resolution equal to 2×2 pixels and one-look speckle statistics. Recall that speckle is a multiplicative noise effect which arises due to the coherent nature of SAR (Porcello, et al.,

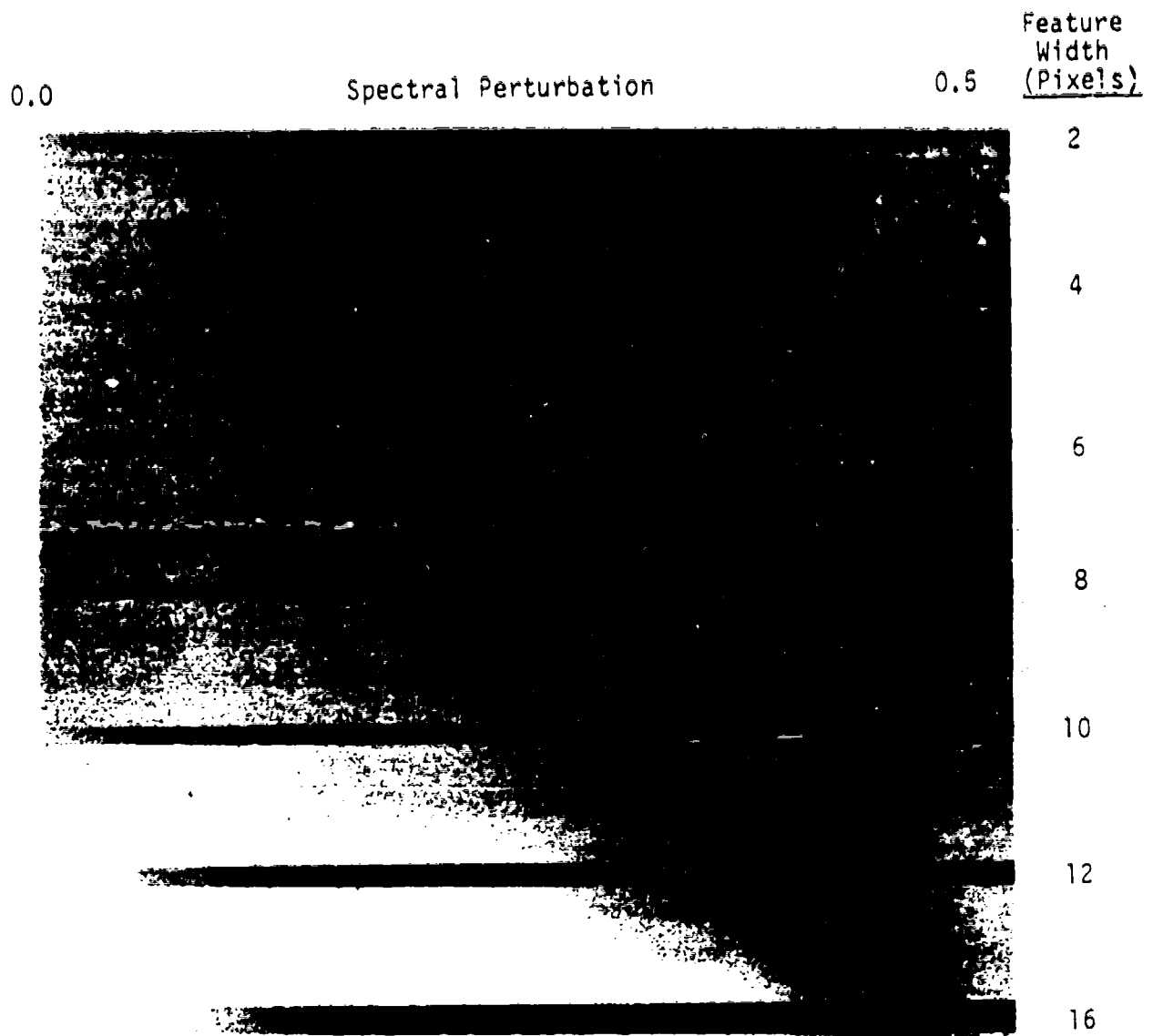


Figure A-1. Spectral Perturbation Pattern Used in SAR Simulations

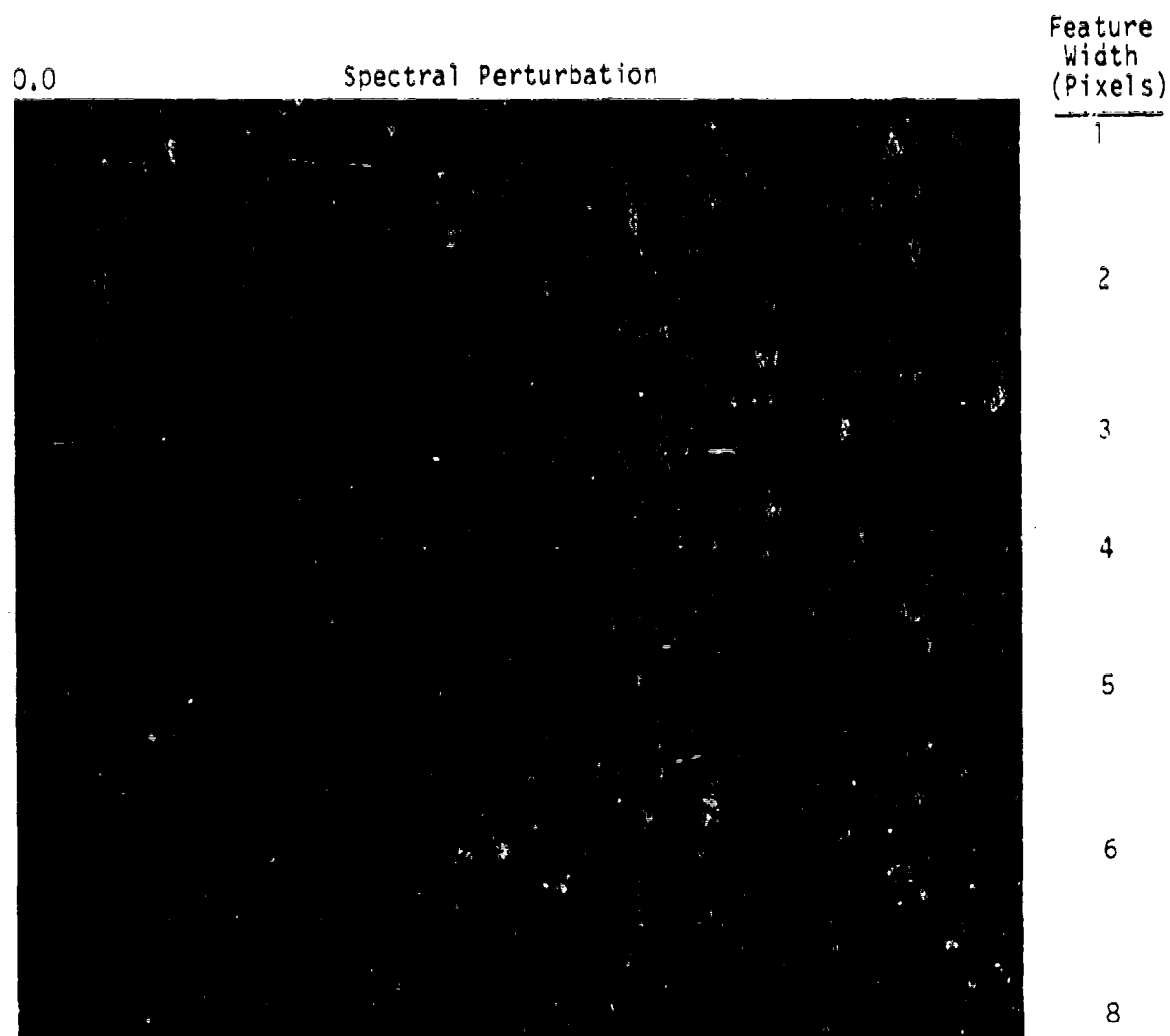


Figure A-2. One-Look Simulated SAR Image Illustrating the Detectability of Wake Features as a Function of Spectral Perturbation and Width

1976). This image indicates several things. The narrowest perturbed region is not visible in the image, even for the highest perturbation values. The wider features are detectable at various perturbation values with the widest features being visible at the smallest perturbations. To accurately determine at what perturbation a feature in this image becomes detectable, the image should be examined from left to right with the right hand portion (large perturbation region) covered. From Figure A-2, it appears that a perturbation of about 0.15 ± 0.05 is detectable for line widths greater than about 6 resolution cells. A four-look simulation of the pattern in Figure A-1 is shown in Figure A-3. The resolution for this simulation was again assumed to be 2×2 pixels. The standard deviation of the speckle in the four-look data is reduced by a factor of two over the one-look data. This improves the detectability of the various features. The narrowest feature is now visible at high perturbations. The minimum detectable perturbation now appears to be about 0.075 ± 0.025 for image features wider than six resolution cells.

Models of detectability based on matched filter theory (Lyzenga, 1985) suggest that the index

$$D = \left[\frac{1}{\rho_x \rho_y} \iint \left(\frac{\Delta \sigma}{\sigma} \right)^2 dx dy \right]^{1/2} \quad (A-1)$$

where $(\Delta \sigma / \sigma)$ represents the pattern strength and $\rho_x \rho_y$ represent the SAR resolution, can be used to estimate detectability. Specifically, a value of D in the order of 15 has postulated as a threshold for visual detectability of internal wave patterns in cases where speckle noise dominates the background visibility.

For a linearly increasing pattern strength as used in the simulations presented here, the detectability index for the portion of the pattern to the left of the position X may be written as

$$D(X) = \frac{X_0}{\rho} \left[\frac{W}{3X_0} \left(\frac{X}{X_0} \right)^3 \right]^{1/2} \quad (A-2)$$

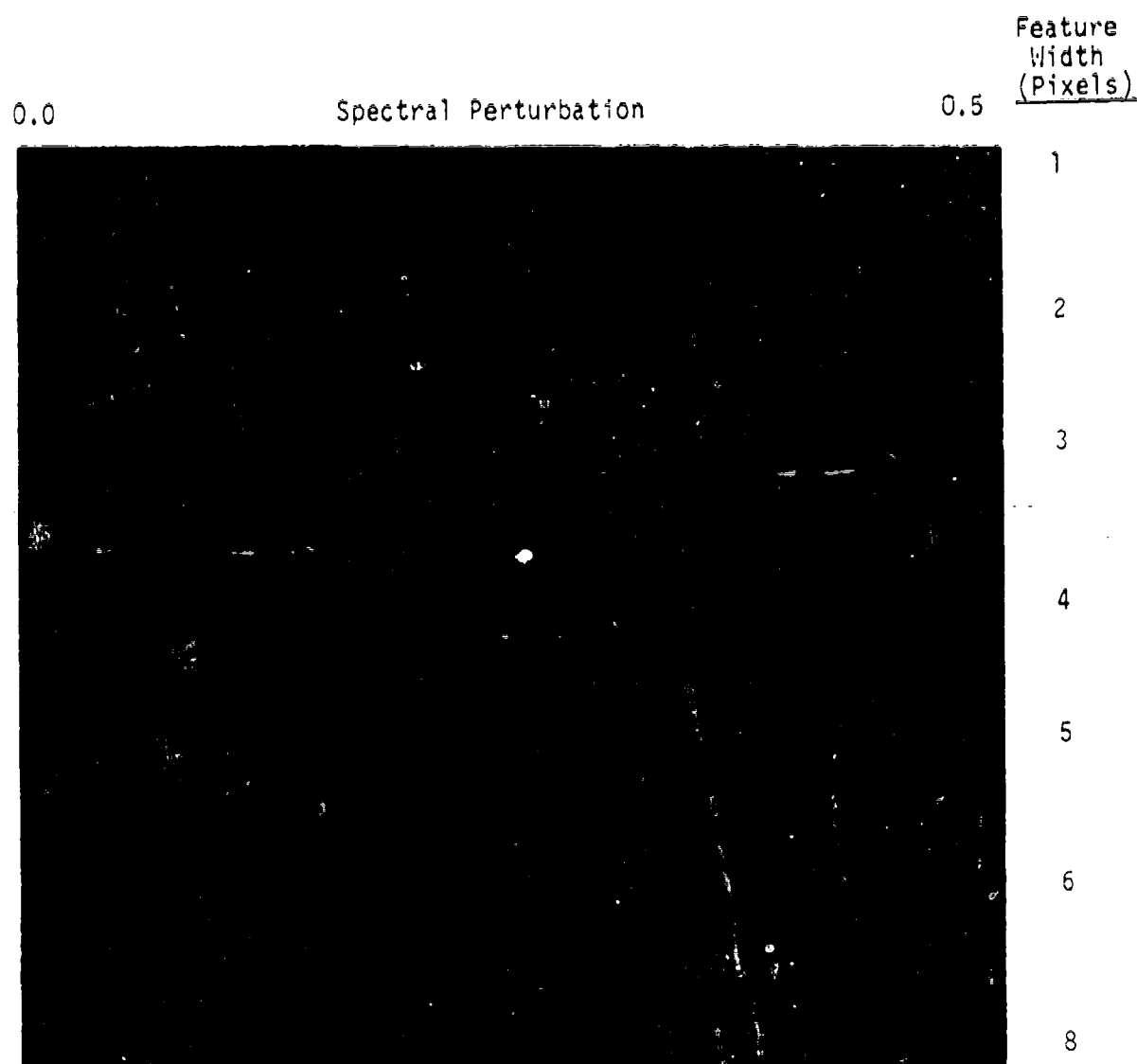


Figure A-3. Four-Look Simulated SAR Image Illustrating the Detectability of Wake Features as a Function of Spectral Perturbation and Width

where W is the pattern width, ρ is the SAR resolution, and X_0 is the position at which $\Delta\sigma/\sigma = 1$. Comparison of this index with the simulated images shows that the patterns become visible where $D \approx 4$, which is the theoretical limit for detectability using a matched filter. The reason for the lower apparent threshold of detectability for these patterns (as opposed to internal wave patterns) is their simpler shape. That is, a pattern consisting of a single line is more easily detectable than a more complicated pattern having the same perturbation strength and area.

Our final simulation also corresponded to the perturbation pattern shown in Figure A-1, but was performed assuming a resolution equal to one pixel and one-look speckle statistics. The resulting image is shown in Figure A-4. This image appears very similar to the four-look simulation in Figure A-3, even though the variance is twice as high. This is a result of the viewer's eye performing the non-coherent integration (multi-looking) of the imagery. The image shown in Figure A-4 would be identical to Figure A-3 if it was smoothed using a 2 by 2 pixel boxcar filter. In other words, this image is the one-look equivalent to Figure A-3 (i.e., both images have the same bandwidth). The four-look equivalent to Figure A-2 would have a resolution of 4 by 4 pixels.

In summary, we have performed the simulations presented above to show the effects of target size, SAR resolution, and speckle, on the detectability of features with varying spectral perturbations. These simulations show that features become more detectable with increasing size, increasing spectral perturbation, and finer resolution or increasing number of looks.

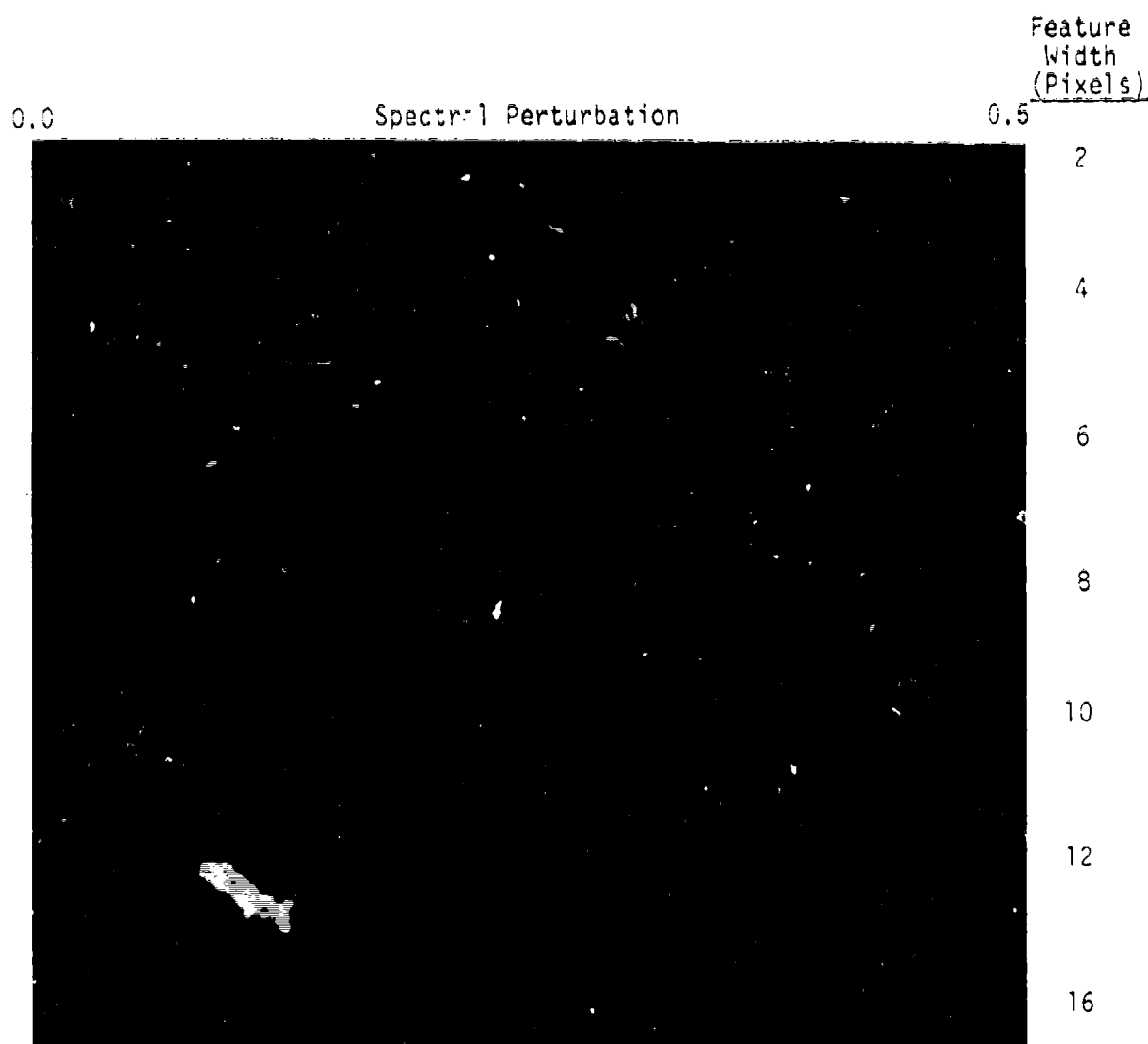


Figure A-4. Higher Resolution One-Look Simulated SAR Image
Illustrating the Detectability of Wake Features as a
Function of Spectral Perturbation and Width

REFERENCES

Fu, L.L. and B. Holt, Seasat Views Oceans and Sea Ice with Synthetic Aperture Radar, JPL Publication No. 81-120, Pasadena, CA, 200 pp., 1982.

Hughes, B.A., The Effect of Internal Waves on Surface Wind Waves, 2, Theoretical Analysis, J. Geophys. Res., 83, 455-465, 1978.

Lyden, J.D., D.R. Lyzenga, R.A. Shuchman, and E.S. Kasischke, Analysis of Narrow Ship Wakes in Georgia Strait SAR Data, ERIM Topic Report No. 155900-20-T, Ann Arbor, MI, 118 pp., 1985a.

Lyden, J.D., Analysis of Seasat Revolution 407 Ship Wake Data, ERIM Topic Report No. 155900-32-T, Ann Arbor, MI, 17 pp., 1985b.

Lyzenga, D.R., Nonlinear Interactions in the Microwave Sensing of Oceanic Internal Waves, ERIM Internal Technical Note, Ann Arbor, MI, 37 pp., 1984.

Lyzenga, D.R., Factors Influencing the Detectability of Ocean Surface Patterns by Synthetic Aperture Radar, ERIM Technical Memorandum 155900-23-T, Ann Arbor, MI 19 pp., 1985.

Phillips, O.M., The Dynamics of the Upper Ocean, Cambridge Univ. Press, New York, 1977.

Porcello, L.W., N.G. Massey, R.B. Innes, and J.M. Marks, Speckle Reduction in Synthetic Aperture Radars, J. Opt. Soc. Am., 66, pp. 1305-1311, 1976.

Shuchman, R.A., E.S. Kasischke, D.R. Lyzenga, and A. Klooster, SAR Ship Wake Signatures, ERIM Topic Report No. 157700-1-x, Ann Arbor, MI, 122 pp., 1983.

Swanson, C.F., Radar Observability of Ship Wakes, Cortana Corporation Report, Falls Church, VA, 87 pp., 1984.

Valenzuela, G.R., Theories for the Interaction of Electromagnetic and Oceanic Waves - A Review, Boundary-Layer Meteorol., 13, pp. 61-85, 1978.